

FILE COPY

4

AD-A227 032

David Taylor Research Center

Bethesda, MD 20084-5000

DTRC-90/014 May 1990

Ship Electromagnetic Signatures Department
Research and Development Report

Radar Cross Section Calculations of Traveling Surface Waves

by

Yuri J. Stoyanov

Clifford R. Schumacher

Aleksandr J. Stoyanov

DTRC-90/014 Radar Cross Section Calculations of Traveling Surface Waves



DTIC
ELECTE
SEP 20 1990
S
E
D
Co

Approved for public release; distribution is unlimited.

90 01 012

MAJOR DTRC TECHNICAL COMPONENTS

- CODE 011 DIRECTOR OF TECHNOLOGY, PLANS AND ASSESSMENT
- 12 SHIP SYSTEMS INTEGRATION DEPARTMENT
 - 14 SHIP ELECTROMAGNETIC SIGNATURES DEPARTMENT
 - 15 SHIP HYDROMECHANICS DEPARTMENT
 - 16 AVIATION DEPARTMENT
 - 17 SHIP STRUCTURES AND PROTECTION DEPARTMENT
 - 18 COMPUTATION, MATHEMATICS & LOGISTICS DEPARTMENT
 - 19 SHIP ACOUSTICS DEPARTMENT
 - 27 PROPULSION AND AUXILIARY SYSTEMS DEPARTMENT
 - 28 SHIP MATERIALS ENGINEERING DEPARTMENT

DTRC ISSUES THREE TYPES OF REPORTS:

1. **DTRC reports, a formal series**, contain information of permanent technical value. They carry a consecutive numerical identification regardless of their classification or the originating department.
2. **Departmental reports, a semiformal series**, contain information of a preliminary, temporary, or proprietary nature or of limited interest or significance. They carry a departmental alphanumeric identification.
3. **Technical memoranda, an informal series**, contain technical documentation of limited use and interest. They are primarily working papers intended for internal use. They carry an identifying number which indicates their type and the numerical code of the originating department. Any distribution outside DTRC must be approved by the head of the originating department on a case-by-case basis.

UNCLASSIFIED

SECURITY CLASSIFICATION OF THIS PAGE

REPORT DOCUMENTATION PAGE

1a. REPORT SECURITY CLASSIFICATION Unclassified			1b. RESTRICTIVE MARKINGS	
2a. SECURITY CLASSIFICATION AUTHORITY			3. DISTRIBUTION/AVAILABILITY OF REPORT Approved for public release; distribution is unlimited.	
2b. DECLASSIFICATION/DOWNGRADING SCHEDULE			5. MONITORING ORGANIZATION REPORT NUMBER(S)	
4. PERFORMING ORGANIZATION REPORT NUMBER(S) DTRC-90/014			7a. NAME OF MONITORING ORGANIZATION	
6a. NAME OF PERFORMING ORGANIZATION David Taylor Research Center		6b. OFFICE SYMBOL (If applicable) Code 1412	7b. ADDRESS (City, State, and ZIP Code)	
6c. ADDRESS (City, State, and ZIP Code) Bethesda, Maryland 20084-5000			9. PROCUREMENT INSTRUMENT IDENTIFICATION NUMBER	
8a. NAME OF FUNDING/SPONSORING ORGANIZATION Office of the Chief of Naval Research		8b. OFFICE SYMBOL (If applicable) OCNR 10	10. SOURCE OF FUNDING NUMBERS	
3c. ADDRESS (City, State, and ZIP Code) Arlington, VA 22217			PROGRAM ELEMENT NO. 0201152N	PROJECT 1001490 WXE001
			TASK NO. R000N000	WORK UNIT ACCESSION NO. 1-1411-002
11. TITLE (Include Security Classification) Radar Cross Section Calculations of Traveling Surface Waves				
12. PERSONAL AUTHOR(S) Y.J. Stoyanov, C.R. Schumacher, and A.J. Stoyanov				
13a. TYPE OF REPORT Final		13b. TIME COVERED FROM 10-10-88 TO 6-30-90		15. PAGE COUNT 41
14. DATE OF REPORT (YEAR, MONTH, DAY) May 1990				
16. SUPPLEMENTARY NOTATION				
17. COSATI CODES			18. SUBJECT TERMS (Continue on reverse if necessary and identify by block number)	
FIELD	GROUP	SUB-GROUP	Radar cross section, surface wave, ogive, rod, computer algorithm, traveling wave antenna	
19. ABSTRACT (Continue on reverse if necessary and identify by block number) The traveling surface wave phenomenon, a significant echo mechanism for long, smooth bodies, manifests itself in the radar cross section (RCS) pattern of realistic targets for horizontal polarization and grazing angles of incidence. Existing radar cross section models do not take this scattering mechanism into account because none of the presently available theories and methods can treat traveling waves in routine fashion [see E.F. Knott, "A Progression of High-Frequency RCS Prediction Techniques," <i>Proc., IEEE</i> , Vol. 73, No. 2 pp. 252-264 (Feb. 1985)]. Analytical radar cross section models for realistic targets should include this type of scattering in their calculations. This report presents a theory and an efficient method for calculating traveling surface wave contributions on a thin rod and an ogive of arbitrary length. Rectangular flat plate radiation patterns are also briefly considered. The details and necessary expressions for predicting RCS of plates will be given in a future report, where the approach will be extended to a more complex target. The theoretical approach presented here is based on the existing concepts of antenna theory and geometrical theory of diffraction. Radar cross section patterns that include traveling wave contributions for a rectangular flat plate and a rod of equal length are calculated and compared with measurements. The theoretical results and measured data show very good agreement.				
20. DISTRIBUTION/AVAILABILITY OF ABSTRACT <input checked="" type="checkbox"/> UNCLASSIFIED/UNLIMITED <input type="checkbox"/> SAME AS RPT <input type="checkbox"/> DTIC USERS			21. ABSTRACT SECURITY CLASSIFICATION Unclassified	
22a. NAME OF RESPONSIBLE INDIVIDUAL Yuri J. Stoyanov			22b. TELEPHONE (Include Area Code) (202) 227-5772	22c. OFFICE SYMBOL Code 1412

CONTENTS

	Page
Abbreviations	iii
Abstract	1
Administrative Information	1
Introduction	1
Radar Cross Section Resulting from Traveling Waves Excited on the Surface of Virtually One-dimensional Long, Thin Targets	2
Surface Traveling Waves on Radar Targets	2
Traveling Wave Antenna Concepts	3
Numerical Results for a Traveling Wave Antenna	5
Link Between the Traveling Wave Antenna and a Long Thin Rod	8
Derivation of Expressions Governing the Location of Traveling Wave Lobes	10
Numerical Results for Traveling Wave Lobes	14
RCS Equations Governing Traveling Wave Contributions on a Thin Rod of Arbitrary Length	14
Theoretical and Experimental RCS Results for a Long Thin Rod	16
RCS Equation Governing Traveling Wave Contributions on the Ogive	20
Theoretical and Experimental Results for an Ogive	23
RCS Resulting from Traveling Waves Excited on the Surface of Virtually One- and Two-Dimensional Targets	28
Link Between the Traveling Wave Antenna, Rod, and a Flat Plate	28
Conclusion	30
Acknowledgments	31
Appendix	32

FIGURES

1. Traveling wave antenna of length L . The field to be determined is at an arbitrary point P	4
2. E -field radiation pattern for the antenna of Fig. 1. The E -field is versus aspect angle θ for an antenna of length $L = 5\lambda$	6
3. The field radiation pattern for an antenna of length $L = 5\lambda$. The E -field is versus ψ angle.	7
4. The field radiation pattern for traveling wave antenna of length $L = 9\lambda$. The E -field is versus ψ angle.	8
5. The field radiation pattern for a traveling wave antenna of $L = 15\lambda$. The E -field is versus ψ angle.	9

6. The field radiation pattern for the traveling wave antenna of Fig. 1. The E -field is versus ψ angle and antenna length $L = 20\lambda$	10
7. The field radiation pattern for the traveling wave antenna of Fig. 1. The E -field is versus ψ angle and antenna length $L = 39\lambda$	11
8. Radar cross section of a rod of length $L = 39\lambda$ and diameter 0.25λ	12
9. Calculated traveling wave RCS contributions for a rod of length $L = 39\lambda$	17
10. Calculated traveling wave RCS contributions for a rod of length $L = 5\lambda$	18
11. Calculated traveling wave RCS contributions for a rod of length $L = 15\lambda$	19
12. Calculated traveling wave RCS contributions for a rod of length $L = 9\lambda$	20
13. Calculated traveling wave RCS contributions for a rod of length $L = 5\lambda$	21
14. Radar cross section of a rod of length 26.512λ (0.228 m), diameter = 0.00163 m, wavelength $\lambda = 0.0086$ m.	22
15. Geometry of the ogive.	23
16. Radar cross section of an ogive of length $L = 39\lambda$, (effective length 39.948λ for traveling wave), radius $R = 77\lambda$, angle $\alpha = 15^\circ$, frequency $f = 23.85$ GHz. Traveling wave phase velocity = 0.99, reflection coefficient = 0.35, horizontal polarization.	24
17. Calculated traveling wave RCS of an ogive of length 39λ , radius = 77λ , ogive half-angle = 15° , traveling wave relative phase velocity = 0.99, reflection coefficient = 0.7, frequency = 23.85 GHz. Horizontal polarization.	25
18. Calculated traveling wave RCS of an ogive of length 39λ , radius = 77λ , ogive half-angle = 15° , traveling wave relative phase velocity = 0.99, reflection coefficient = 0.32, frequency = 23.85 GHz. Horizontal polarization.	26
19. Radar cross section of an ogive of length = 15.19λ (1.519 m), radius = 0.1 m, ogive half-angle = 15° , traveling wave relative phase velocity = 0.988, reflection coefficient = 0.25, frequency = 3 GHz. Horizontal polarization.	27
20. Radar cross section of an ogive of length = 32λ (effective length 32.9λ), radius = 62λ , ogive half-angle = 14.6° , traveling wave relative phase velocity = 0.99, reflection coefficient = 0.32, frequency = 23.85 GHz. Horizontal polarization.	28
21. Same as Fig. 20, but measured curve is shifted by 3.53 dB.	29
22. Total radar cross section of a $5\lambda \times 0.9725\lambda$ flat rectangular plate (solid line) and the traveling wave RCS contributions of a rod of equal length with diameter 0.25λ (dotted line).	30

ABBREVIATIONS

a	Radius of a rod
a_θ	Components of a unit vector
a_ϕ	
a_r	
$A_r(\theta, \phi)$	Absorption cross section
B	Maximum value of the pattern factor
b_n	Characteristic value for given traveling wave lobe
c	Speed of light
D	Directivity
ΔL	Length increment
E	Electric field vector
E	rms of the electric field strength
F	$kL(1 - \cos \theta)/2$
f	Frequency
$G(\theta, \phi)$	Gain function of the equivalent antenna
GHz	10^9 Hz
H	Magnetic field vector
H_ϕ	Magnetic field component
i	$\sqrt{-1}$
$I, I(z), I(z, t)$	Alternating Current
I_0	Current amplitude
k	Wave number of plane wave in free space
L	Length of a target
L_{eff}	Actual path length
P	Arbitrary point of observation
$p = v/c$	Relative phase velocity of the surface current
R	Ogive radius
r	Radial coordinate of the field point
r'	$r - z \cos \theta$
t	Time
z	Axis or coordinate



Accession For	
NTIS GRA&I	<input checked="" type="checkbox"/>
DTIC TAB	<input type="checkbox"/>
Unannounced	<input type="checkbox"/>
Justification	
By	
Distribution/	
Availability Codes	
Dist	Avail and/or Special
A-1	

α	Ogive half angle
β	$ik(1 - \cos \theta)$
γ	Current reflection coefficient
ϵ	Permittivity
η	Intrinsic impedance
θ	Angular coordinate of the field point
θ_n	Positions of the traveling wave lobes
λ	Wavelength
μ	Permeability
σ	Radar Cross Section (RCS)
ϕ	Spherical polar coordinate
ψ	$90^\circ - \theta$, aspect angle
ω	Angular frequency

FOREWORD

Because many contemporary requirements for radar cross section (RCS) computations are for large, complex targets, the most useful prediction methods lie in the high frequency band. However, a recent survey of high frequency RCS prediction techniques¹ confirmed that none of these methods can adequately handle the surface traveling wave phenomenon, which is a significant echo mechanism for large realistic targets.

The importance of predicting the traveling surface wave phenomenon lies not only in the need to improve existing theory and methods and thereby extend current frontiers of this field, but also in potential valuable applications to realistic targets for the purpose of radar signature prediction, analysis and control. The echo area resulting from traveling waves excited on the surface of targets depends strongly on both the entire surface and the edges bounding the surface.

The great diversity of surface shapes and types of discontinuities, as well as the complexity of proper theoretical formulations for this problem, have made it necessary to approach the solution in a series of steps. Each of these steps is distinct, and each step will be defined and documented in a corresponding report.

This report is the first in the series. It covers that part of the problem which includes radar targets with dominant contributions from traveling surface waves. We consider here a long thin rod and an ogive. The radiation patterns of these targets exhibit strong dependence upon the traveling wave mechanism.

In other reports on this subject we will extend the approach to complex targets whose RCS patterns exhibit contributions from many scattering mechanisms. For these targets the traveling wave contributions are still significant but do not dominate the overall radar scattering. Accurate predictions of the target radar cross section are achieved by adding traveling wave contributions to major scattering mechanisms.

ABSTRACT

The traveling surface wave phenomenon, a significant echo mechanism for long, smooth bodies, manifests itself in the radar cross section (RCS) pattern of realistic targets for horizontal polarization and grazing angles of incidence. Existing radar cross section models do not take this scattering mechanism into account because none of the presently available theories and methods can treat traveling waves in routine fashion [see E.F. Knott, "A Progression of High-Frequency RCS Prediction Techniques," Proc., IEEE, Vol. 73, No. 2 pp. 252-264 (Feb. 1985)]. Analytical radar cross section models for realistic targets should include this type of scattering in their calculations. This report presents a theory and an efficient method for calculating traveling surface wave contributions on a thin rod and an ogive of arbitrary length. Rectangular flat plate radiation patterns are also briefly considered. The details and necessary expressions for predicting RCS of plates will be given in a future report, where the approach will be extended to a more complex target. The theoretical approach presented here is based on the existing concepts of antenna theory and geometrical theory of diffraction. Radar cross section patterns that include traveling wave contributions for a rectangular flat plate and a rod of equal length are calculated and compared with measurements. The theoretical results and measured data show very good agreement.

ADMINISTRATIVE INFORMATION

This project was supported by the Office of Naval Technology and by the David Taylor Research Center's (DTRC) Independent Research and Independent Exploratory Development Program; it was sponsored by the Office of the Chief of Naval Research (OCNR), Director of Naval Research, OCNR 10, Director of Naval Technology OCNR 20; and it was administered by the Research Director, DTRC 0113, Under Program Element 61152N, task Arca ZR-000-01-01 and DTRC Work Units 1-1411-002 and 1-2844-120.

INTRODUCTION

Many contemporary requirements for radar cross section (RCS) calculations are for large, complex targets and are in the high frequency band. Furthermore, radar scattering from any realistic target is a function of the body's material properties as well as its geometry. Once the specular reflections have been eliminated by radar absorbing materials, only nonspecular or diffractive sources are left. Nonspecular scatterers are edges, creeping waves, and traveling waves. They often dominate backscattering patterns of realistic targets in the aspect ranges of most interest. To suppress these sources as well, an accurate and computationally efficient theoretical formulation must be found to predict them, and then the effect of the target's material properties on such nonspecular sources must be examined. While our repertory of useful computation methods has been greatly expanded in the last 50 years, some scattering mechanisms, such as traveling surface wave phenomena, still cannot be treated in routine fashion (Knott¹). A growing effort directed at this type of scattering has been seen in the past few years.² However, none of the presently available methods can adequately handle the traveling surface wave.

This report is the first of a series which will describe research to develop an accurate and computationally efficient theoretical formulation for predicting traveling surface

waves. The objective of this program was to study and analyze nonspecular scattering and to find the most effective methods in suppressing its contributions to the backscattering from various target shapes. For most targets of interest, nonspecular scattering due to traveling surface waves takes place at horizontal polarization, and the trailing edge of the target is the dominant source of scattering.

Three typical geometries were selected for study: a long thin rod, an ogive and a flat rectangular plate. The rod and the ogive are discussed in detail in this report; the rectangular plate will be dealt with in a future report.* Measured radar cross section patterns of such targets are available in the open literature.^{3,4} Although we have considered only three shapes, the results obtained are applicable to targets of different geometries as well.

The analogy was explored between a traveling wave antenna and the three geometries selected in order to derive equations for predicting radiation patterns. The end-fire antenna theory was applied here for the purpose of studying the traveling wave mechanism. The geometric similarity between the traveling wave antenna and the selected targets manifests itself also in the radiation patterns. The traveling wave antenna is simple for analysis because its characteristics are well controlled and its theory is well established.

First the Maxwell equations were applied in the theoretical treatment of a traveling wave antenna. Expressions were derived for calculating the antenna field radiation pattern. The analogy was then explored between the calculated antenna radiation patterns and the traveling wave echo returns in radar cross section patterns of realistic targets. The antenna equations obtained were used initially to derive expressions for predicting traveling wave contributions to RCS patterns of virtually one dimensional targets such as a long thin rod and an ogive. Finally, we have briefly discussed extension of this theory to a flat rectangular plate.

RADAR CROSS SECTION RESULTING FROM TRAVELING WAVES EXCITED ON THE SURFACE OF VIRTUALLY ONE-DIMENSIONAL LONG, THIN TARGETS

SURFACE TRAVELING WAVES ON RADAR TARGETS

The traveling wave is a high frequency phenomenon. Surface traveling waves are launched for horizontal polarization and grazing angles of incidence on targets with long smooth surfaces. There is little attenuation from the flat smooth surface, so the wave builds up as it travels along the target. Upon reaching a surface discontinuity, for example an edge, the traveling wave is scattered and part of it propagates back toward the radar. The sum of the traveling waves propagating from the far end of the target toward the near end is the dominant source to the target radar cross section. This can be clearly observed in the radiation pattern of a long thin rod. The radar return of the rod is small if the incident electric field is perpendicular to the axis, but the return is large if the electric field is in the plane containing the propagation vector and the rod axis. Moreover, as will be shown in the next section, the shape of the radiation pattern from a traveling wave

*Stoyanov, Y.J., C.R. Schumacher, and A.J. Stoyanov, "Radar Cross Section Calculation of Traveling Surface Waves on a Flat Rectangular Plate," DTRC report in preparation.

antenna is very similar to the part of the radar cross section pattern of the rod that is due to traveling wave contributions. The same physical mechanism is behind both cases.

The traveling wave echo area from the far end point of a rod and an ogive were treated by Peters³ in 1958. However, this treatment is approximate, and little progress has been made since this work was published. The treatment has not been extended to the routine calculation of surface traveling waves for more complex realistic targets. To derive expressions that can be used in routine calculations of RCS by computer models that include traveling surface wave contributions, we have developed methods that incorporate and extend information currently available on traveling surface waves. We have established stable relations between target dimensions and radar frequency. Our approach includes traveling wave antenna concepts and expressions used to predict traveling wave lobes.

TRAVELING WAVE ANTENNA CONCEPTS

The theory of traveling wave antennas is based upon Maxwell's equations. If damping due to radiation emission is neglected and the antenna is thin enough, the current along the antenna can be taken as sinusoidal in time and space with wave number $k = \omega/c$ where ω is the angular frequency and c is the speed of light. For currents $I(z, t)$ varying in time we can make a Fourier analysis of the time dependence and handle each Fourier component separately:

$$I(z, t) = I(z)e^{-i\omega t}$$

In the equations that follow the time dependence factor, $e^{-i\omega t}$, is assumed and is omitted for brevity. For the traveling wave antenna the geometry of current flow is simple enough that the integral for the vector potential is found in closed form.

Consider a thin, linear antenna of length L (shown in Fig. 1). The antenna is assumed to be oriented along the z -axis. This antenna is fed at $z = 0$, and its far end ($z = L$) is grounded. For the antenna shown in Fig. 1 there is only a traveling wave in the $+z$ direction caused by the alternating current.

$$I(z) = I_0 \exp(-ikz) . \quad (1)$$

Such an antenna generates traveling wave radiation patterns. Maxwell equations are applied first to a short antenna whose length L is much less than the incident wave length ($L < \lambda$). The radiation expressions derived for a short antenna are then used to develop solutions for a long antenna with ($L \gg \lambda$). The electric field strength at point $P(r \ll \lambda)$ is given by⁵

$$\mathbf{E} = \frac{-i}{\omega \epsilon} \nabla \times \mathbf{H} , \quad (2)$$

where \mathbf{E} and \mathbf{H} are electric and magnetic field strength vector, respectively, and they are a function of space variables only.

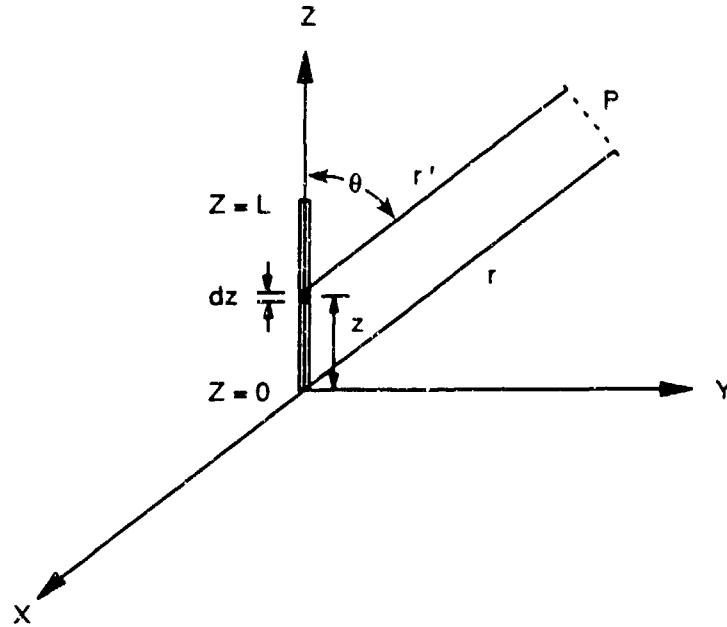


Fig. 1. Traveling wave antenna of length L . The field to be determined is at an arbitrary point P .

$$\nabla \times \mathbf{H} = \frac{a_r}{r \sin \theta} \frac{\partial}{\partial \theta} (H_\phi \sin \theta) - \frac{a_\theta}{r} \frac{\partial}{\partial r} (r H_\phi) , \quad (3)$$

$$\mathbf{H} = a_\phi \frac{I(z)}{4\pi} \left[\frac{2\pi i}{r\lambda} + \frac{1}{r^2} \right] \sin \theta \Delta L e^{-ikr} . \quad (4)$$

In these equations \mathbf{E} has components in both r and θ directions, while \mathbf{H} is always in the ϕ -direction.

Substituting Eq. 4 into Eq. 3 and then into Eq. 2, and noting that for large distances to the point P ($r \gg L$) we can ignore terms containing the negative second and third power of r , we obtain:

$$dE = a_\theta \frac{i\omega\mu I(z)}{4\pi r'} \sin \theta \exp\left(\frac{-i2\pi r'}{\lambda}\right) dz , \quad (5)$$

where $r' = r - z \cos \theta$ and dz is an infinitesimal element of the antenna length.

Substituting Eq. 1 into the above Eq. 5, we obtain

$$dE \approx a_\theta \frac{i\omega\mu I_0}{4\pi r} \sin \theta \exp\left[-ik\left[r + z(1 - \cos \theta)\right]\right] dz . \quad (6)$$

The electric field at P from the whole antenna of length L is obtained by integrating from $z = 0$ to $z = L$:

$$E \approx a_\theta \frac{i\omega\mu I_0}{4\pi r} \sin \theta \exp(-ikr) \int_0^L \exp[-ikz(1 - \cos \theta)] dz. \quad (7)$$

Evaluating the integral in this equation we obtain

$$\int_0^L \exp[-ikz(1 - \cos \theta)] dz = -\frac{1}{\beta} \int_0^L \exp(-\beta z) d(-\beta z) = (1 - e^{-\beta L}) \frac{1}{\beta}, \quad (8)$$

where $\beta = ik(1 - \cos \theta)$ and $k = 2\pi/\lambda$.

Substituting Eq. 8 into Eq. 7, we obtain

$$E \approx a_\theta \frac{i\omega\mu}{4\pi r} I_0 e^{-ikr} \sin \theta \frac{[1 - e^{-ik(1 - \cos \theta)L}]}{ik(1 - \cos \theta)}$$

or

$$E \approx a_\theta \frac{\omega\mu\lambda}{2\pi} \frac{I_0 e^{-ikr}}{4\pi r} \frac{\sin \theta}{(1 - \cos \theta)} [1 - e^{-ik(1 - \cos \theta)L}].$$

Since $k = \frac{2\pi}{\lambda} = \omega \sqrt{\mu\epsilon}$ and $\eta = \sqrt{\frac{\mu}{\epsilon}} = \frac{\omega\mu\lambda}{2\pi}$, we can rewrite the above equation in a compact form:

$$E \approx a_\theta \frac{\eta I_0 e^{-ikr}}{4\pi r} \frac{\sin \theta}{(1 - \cos \theta)} [1 - e^{-i2F}] \quad (9)$$

where $F = kL(1 - \cos \theta)/2$.

To calculate the radiation pattern at point P for the traveling wave antenna under discussion, we can use the rms magnitude of the electric field strength given by Eq. 9

$$|E| = \frac{\eta I_0}{2\pi r} \left| \frac{\sin F \sin \theta}{1 - \cos \theta} \right|. \quad (10)$$

The derivation of Eq. 10 is given in the Appendix.

Equation 10 shows that the rms amplitude of the E-field is a function of aspect angle θ , antenna length L , and incident wave length λ , for a given values of r , η , and I_0 .

NUMERICAL RESULTS FOR A TRAVELING WAVE ANTENNA

Figure 1 provides the geometry of the problem. The electromagnetic field at an arbitrary point P is produced by the alternating current which gives rise to the surface wave traveling along the antenna length. The radiation field patterns at point P are calculated by using Eq. 10. However, since we are primarily interested in the dependence of

radiation pattern on antenna length (expressed in terms of wavelength), Eq. 10 is modified to become

$$|E| = \text{const} \left| \frac{\sin \theta \sin \left[\pi(1 - \cos \theta) \frac{L}{\lambda} \right]}{1 - \cos \theta} \right|. \quad (11)$$

For a given antenna of length L the constant can be set equal to unity. Figure 2 shows the calculated radiation pattern (i.e. $|E|$ - field versus aspect) for the antenna of length $L = 5\lambda$. The lobe structure consists of five peaks. The maximum radiation occurs at the principal lobe, which for the antenna of given length ($L = 5\lambda$) occurs at $\theta = 22.1^\circ$ (i.e. $\psi = 90^\circ - \theta = 67.9^\circ$) (Fig. 3). This pattern is the same radiation pattern as that in Fig. 2, but it is for angle ψ , which is used later in the text for easy comparison with rod and flat plate RCS patterns.

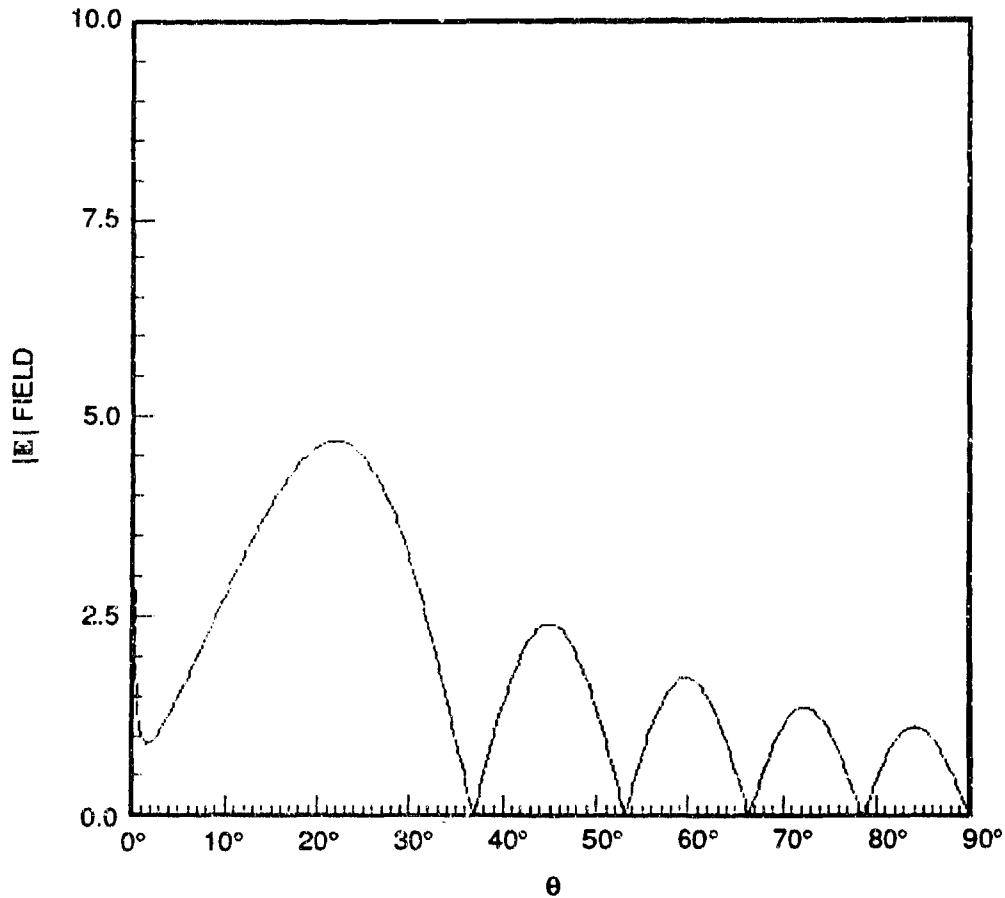


Fig. 2. E -field radiation pattern for the antenna of Fig. 1. The E -field is versus aspect angle θ for an antenna of length $L = 5\lambda$.

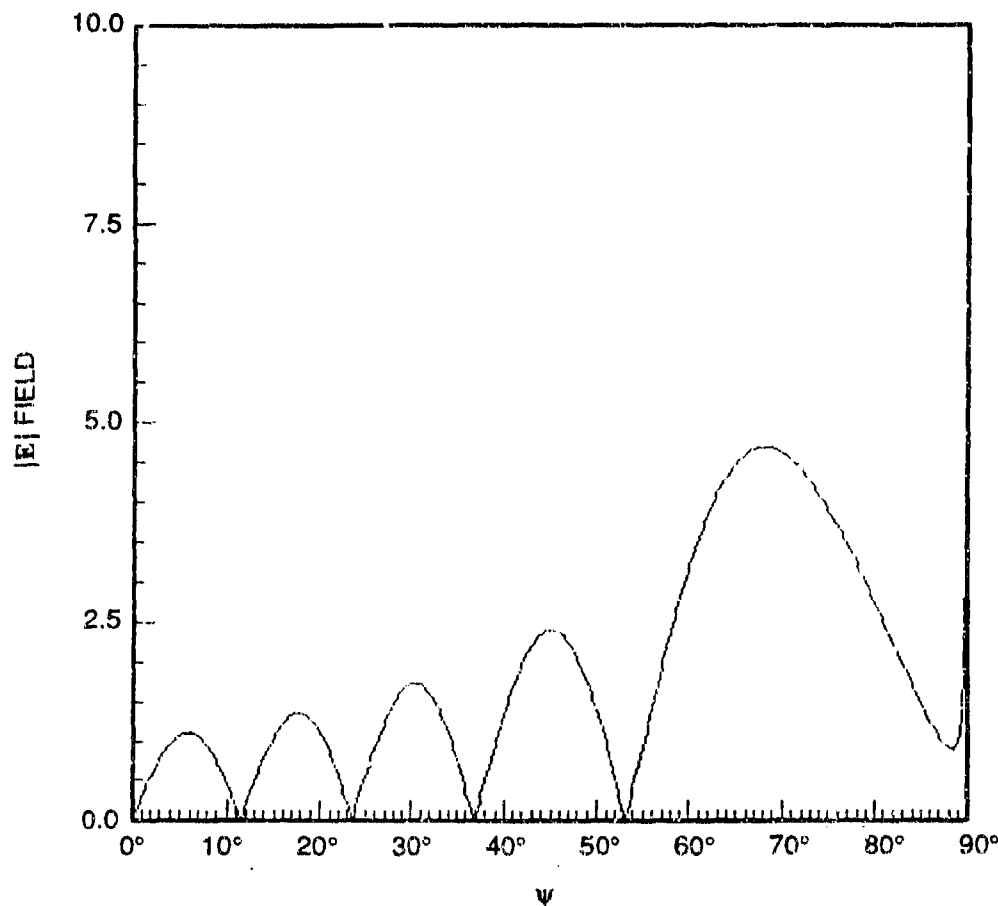


Fig. 3. The field radiation pattern for an antenna of length $L = 5\lambda$. The E -field is versus ψ angle.

For a longer antenna, such as $L = 9\lambda$, the radiation field pattern is shown in Fig. 4. The lobe structure due to the traveling wave consists of nine peaks for this antenna. Again the maximum radiation occurs at the principal lobe, which for the antenna of $L = 9\lambda$ occurs at $\psi = 73.5^\circ$ (i. e. at $\theta = 16.5^\circ$).

Figure 5 shows the calculated field pattern for an antenna of length $L = 15\lambda$. This radiation pattern has 15 lobes. The maximum radiation comes from the principal lobe, which occurs at $\theta = 12.7^\circ$ ($\psi = 77.3^\circ$). Figures 6 and 7 show calculated field radiation patterns for antennas of 20 and 39 wavelengths, respectively. These figures show that the number of lobes exactly corresponds to the antenna length in terms of wavelength. The principal lobes for antennas having a length of 20 and 39 wavelengths occur at $\theta = 11.0^\circ$ ($\psi = 79.0^\circ$) and $\theta = 7.9^\circ$ ($\psi = 82.1^\circ$), respectively.

These examples indicate that as an antenna increases in length for a fixed λ , the number of lobes in the field radiation pattern increases and the principal lobe shifts to a

region of a very low θ angles of incidence ($\theta = 90^\circ - \psi$). The arguments just presented are next used to predict lobe locations and to derive and verify analytical formulas. As was mentioned earlier, the ability to calculate the location of the principal lobe in the radiation pattern represents a significant link between antenna theory and a realistic target echo area, and this link is important in predicting traveling wave contributions to the radar cross section of the target.

LINK BETWEEN THE TRAVELING WAVE ANTENNA AND A LONG THIN ROD

Next the traveling wave antenna radiation pattern shown in Fig. 7 is compared with the measured RCS plot of Fig. 8 for a long thin rod of equal length ($L = 39\lambda$). The RCS patterns and equations of realistic targets usually differ from the antenna E -field radiation pattern and corresponding antenna equation in many ways, but they do have one common feature: the traveling surface wave. Indeed, the traveling wave antenna is the only target whose radiation pattern results from the traveling wave mechanism. The radiation pattern of a long thin rod results from two dominant scattering mechanisms, specular reflection

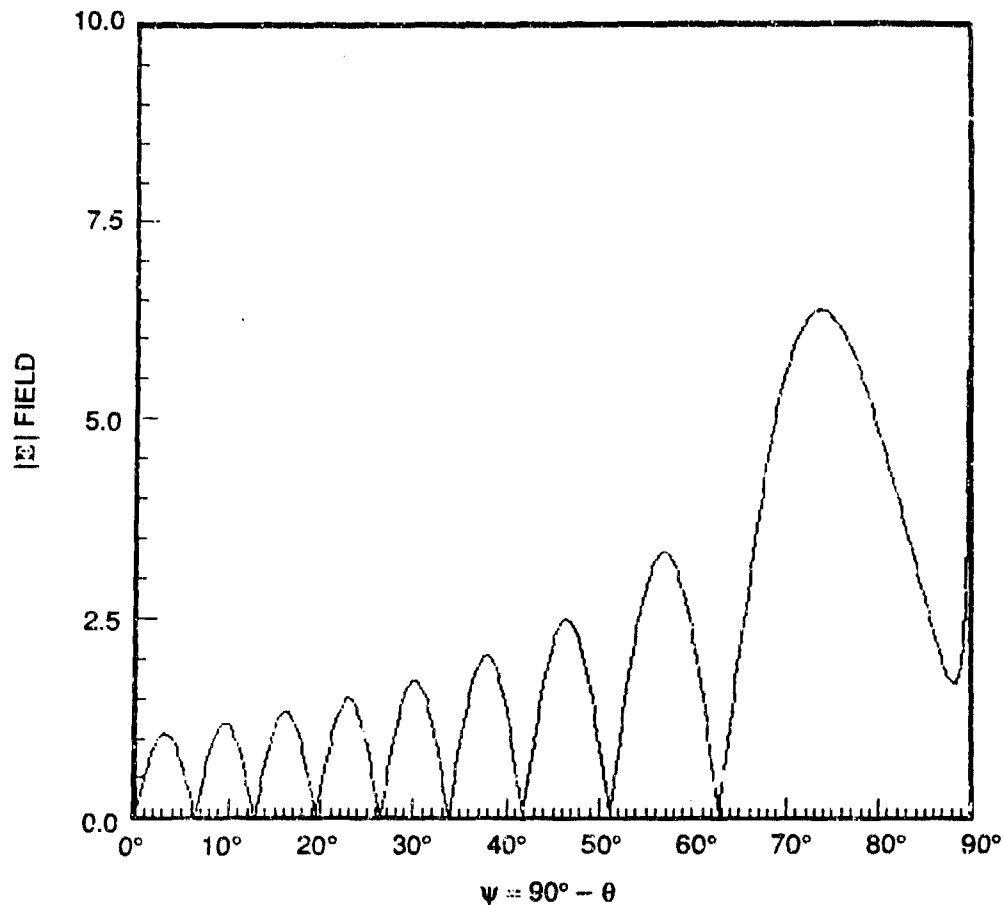


Fig. 4. The field radiation pattern for traveling wave antenna of length $L = 9\lambda$. The E -field is versus ψ angle.

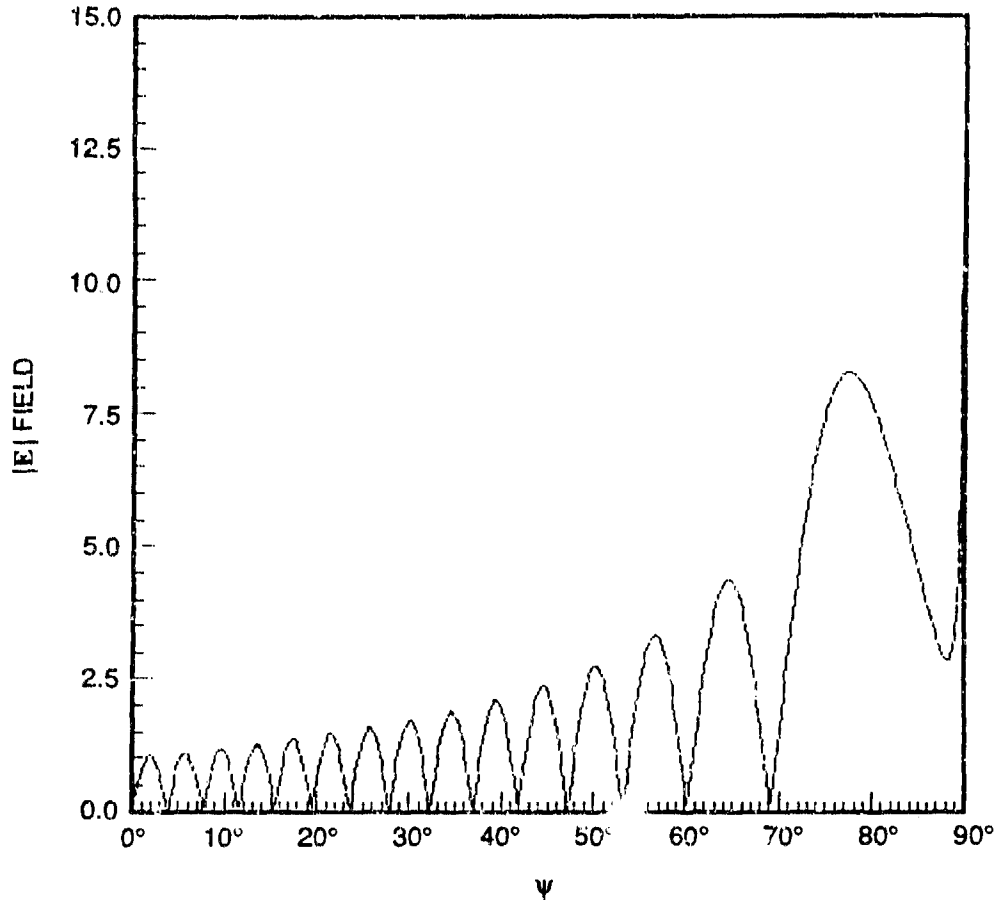


Fig. 5. The field radiation pattern for a traveling wave antenna of $L = 15\lambda$. The E -field is versus ψ angle.

and the traveling surface wave. Targets of more complex shape exhibit more scattering mechanisms. Therefore, to study the traveling wave phenomenon we first considered radar targets having the minimum number of scattering mechanisms besides the traveling wave.

The plot for the rod RCS has two peaks at or near $\theta = 0^\circ$ and $\theta = 90^\circ$. At a grazing angle of incidence the traveling wave contributions for the rod represent a lobe structure whose shape agrees well with the traveling wave antenna radiation pattern of Fig. 7. To develop a traveling wave theory that can be used to predict rod RCS patterns we explored the possibility of using Eq. 10 of the traveling wave antenna and the remarkable similarity in radiation patterns observed in the previous section. Since Eq. 10 is not directly applicable in calculations of the rod RCS, we have derived equations that are in agreement with the antenna lobes, and hence preserve the lobe structure. These equations can be used to predict the traveling wave lobe positions.

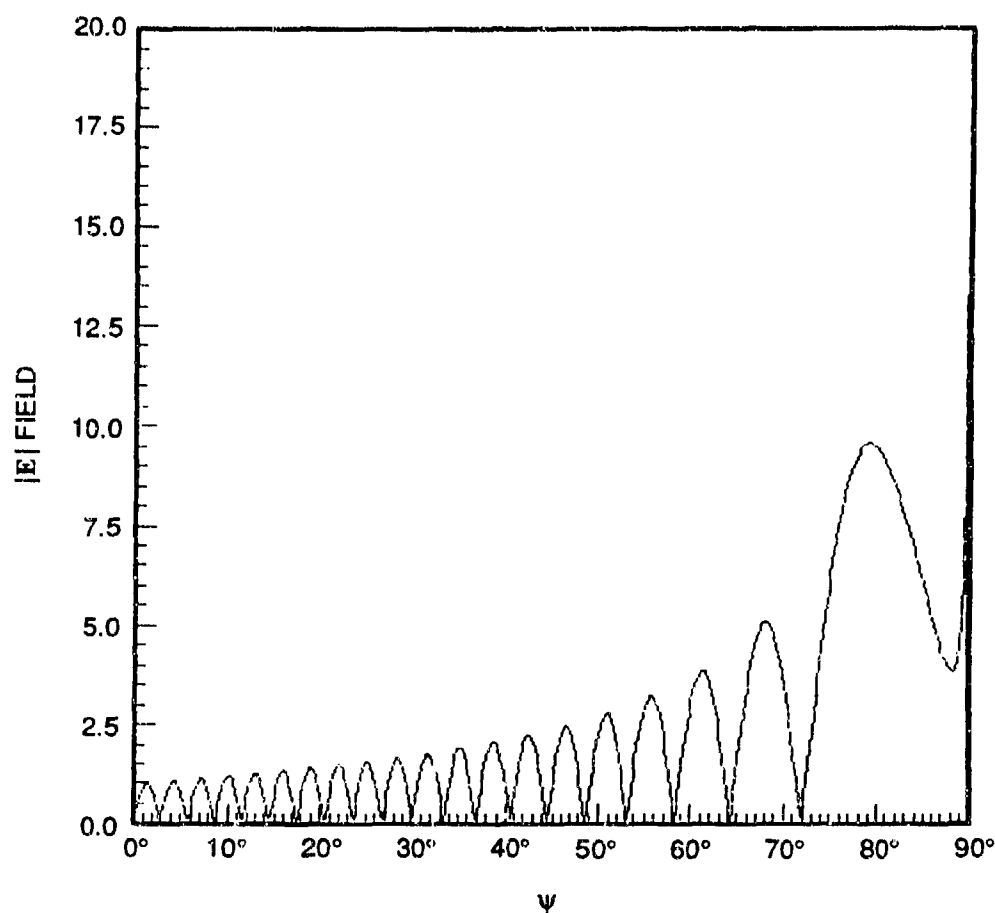


Fig. 6. The field radiation pattern for the traveling wave antenna of Fig.1. The E -field is versus ψ angle and antenna length $L = 20\lambda$.

DERIVATION OF EXPRESSIONS GOVERNING THE LOCATION OF TRAVELING WAVE LOBES

Having identified the traveling wave mechanism as the link between the traveling wave antenna radiation pattern Eq. 10 and the rod RCS pattern, we next derived the expressions that govern the location of traveling wave lobes for realistic targets such as a thin rod and an antenna. We have re-examined Eq. 10 in this section to derive the equation that can be used to predict lobe positions directly, without calculating radiation patterns and then reading out the lobe positions. This is accomplished by differentiating Eq. 10 with respect to θ and then setting the result to be equal zero. Thus,

$$\frac{d|E|}{d\theta} = \frac{\eta I}{2\pi r} \frac{d}{d\theta} \left| \frac{\sin F \sin \theta}{1 - \cos \theta} \right| = 0$$

$$\sin F \left[\frac{\cos \theta}{1 - \cos \theta} - \frac{\sin^2 \theta}{(1 - \cos \theta)^2} \right] + \frac{\sin^2 \theta}{1 - \cos \theta} \cos F \frac{dF}{d\theta} = 0 ,$$

where $F = kL(1 - \cos \theta)/2$, and

$$\frac{dF}{d\theta} = \frac{d}{d\theta} [kL(1 - \cos \theta)/2] = \frac{kL}{2} \sin \theta .$$

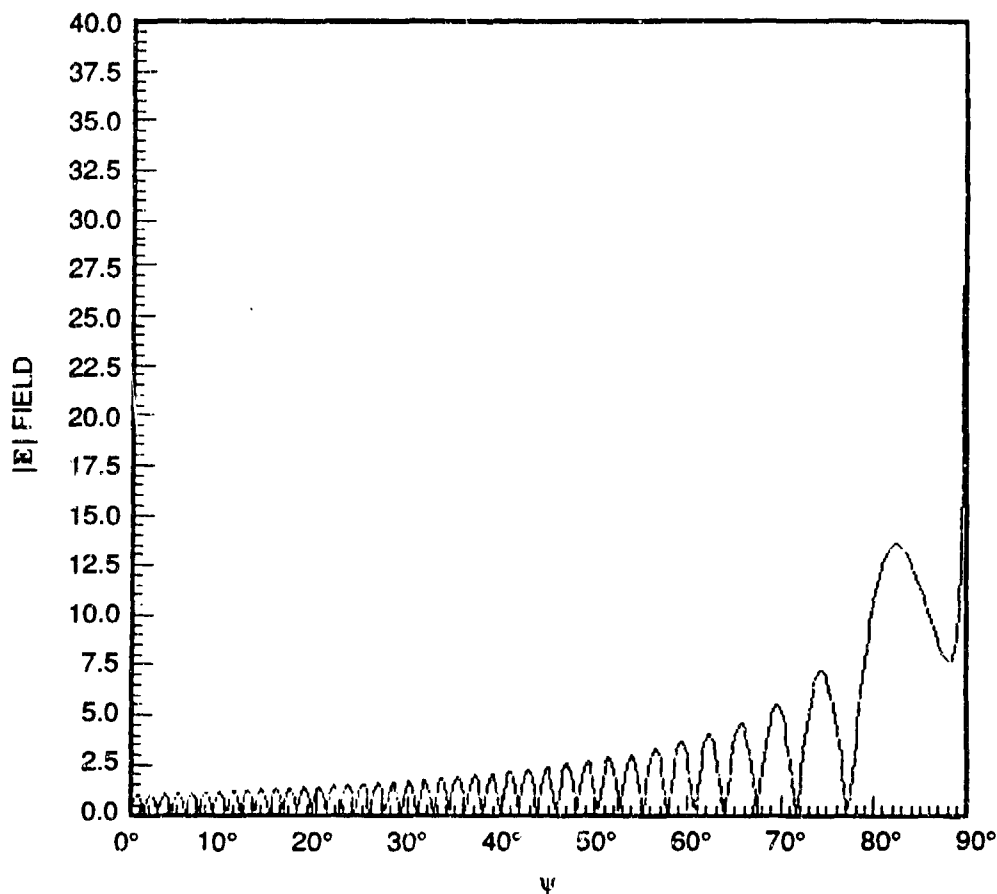


Fig. 7. The field radiation pattern, for the traveling wave antenna of Fig.1. The E -field is versus ψ angle and antenna length $L = 39\lambda$.

Hence,

$$\tan F = \left[-\frac{kL \sin^2 \theta}{2} \right] / \left[(1 - \cos \theta) / \left(\frac{\cos \theta}{1 - \cos \theta} - \frac{\sin^2 \theta}{(1 - \cos \theta)^2} \right) \right]$$

$$= \frac{kL}{2} \sin^2 \theta . \quad (12)$$

Thus, Eq. 12 can be used to predict the exact position of the lobes in the RCS plot of the rod and the antenna. This equation contains two variables: θ and L (expressed in wavelengths). The solution of such a transcendental equation can be found numerically by substituting various values of θ , or by using available computer algorithms based on the method of successive approximation. By using Eq. 12, we can predict the main radiation peak to be at $\theta = 34.9^\circ$ for an antenna of length $L = 2\lambda$, and at $\theta = 22.1^\circ$ for the antenna of length $L = 5\lambda$.

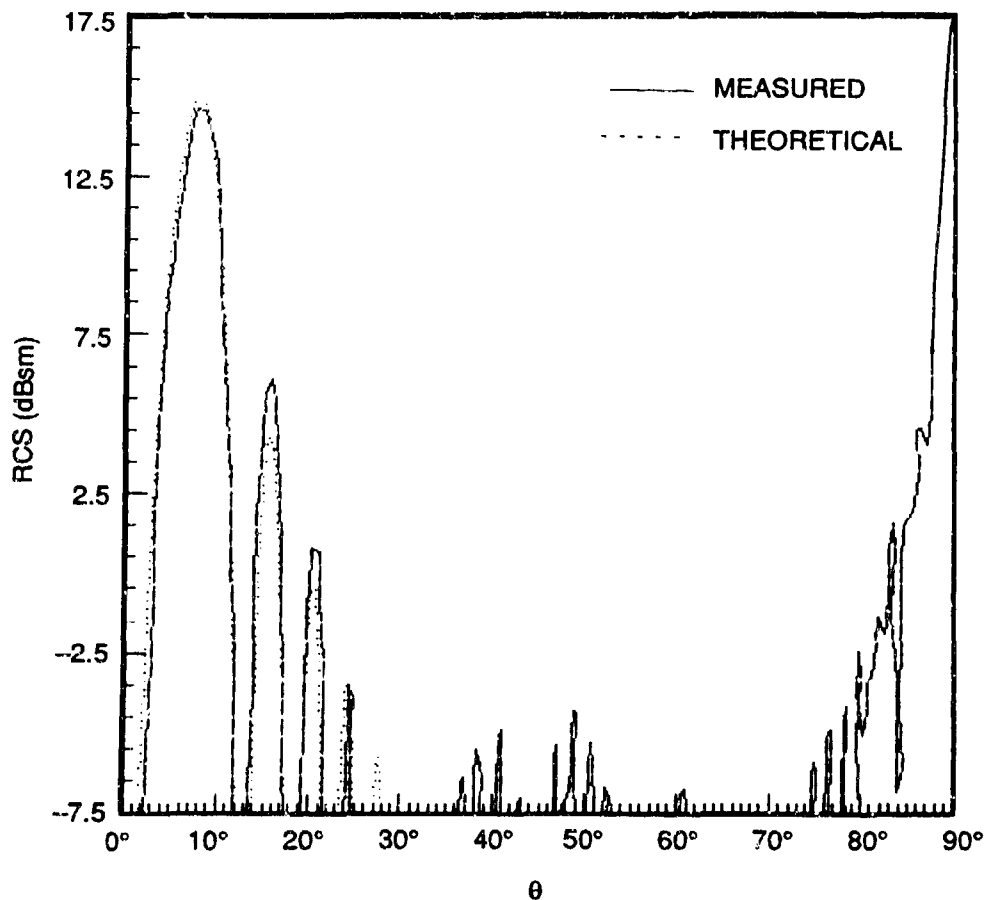


Fig. 8. Radar cross section of a rod of length $L = 39\lambda$ and diameter 0.25λ . Frequency = 23.85 GHz. Horizontal polarization. Traveling wave relative phase velocity = 1.0 and reflection coefficient = 0.32. Calculated traveling wave RCS contributions are shown by dotted line; measured (solid) curve is taken from Peters.³

These and other solutions of Eq. 12 can be verified by comparing them with the plots calculated in the previous section from Eq. 10. Figures 2 to 5 show field radiation patterns for antennas of length $L = 2\lambda$, 9λ , 15λ , and 20λ , respectively. These plots show that the maximum radiation peak is the first or principal lobe at $\theta = 22.1^\circ$, $\theta = 16.5^\circ$, $\theta = 12.7^\circ$, and $\theta = 11.0^\circ$. For the antenna of length $L = 5\lambda$ the agreement is excellent. The second, third and other lobes can be found from these plots or from the following relation:

$$\theta_n \cong \frac{360^\circ}{\pi} \sqrt{\frac{b_n}{2\pi}} \sqrt{\frac{\lambda}{L}}, \quad (13)$$

where θ_n is the azimuth position of the n th lobe and b_n is the characteristic value for the given lobe. The numerical value of b_n can be found from plots of Eq. 10 calculated for the antenna of given length or by numerical means (Knott et al.⁶). For each lobe the b_n values can also be found by using Eq. 14:

$$b_n = \frac{2L}{\lambda} \pi^3 \left(\frac{\theta_n}{360^\circ} \right)^2. \quad (14)$$

For the first three large lobes the angles θ_1 , θ_2 , and θ_3 can be accurately determined from the antenna radiation plots. Thus, $b_1 = 1.1555$, $b_2 = 4.604$, and $b_3 = 7.7898$. For example, reading the θ_n values from Fig. 7 ($L = 39\lambda$) and then substituting them in Eq. 14 gives the b_n values. Substituting b_n values into Eq. 13 we obtain, in turn,

$$\theta_1 = 49.35 \sqrt{\frac{\lambda}{L}}, \quad (15)$$

$$\theta_2 = 98.09 \sqrt{\frac{\lambda}{L}}, \quad (16)$$

$$\theta_3 = 127.59 \sqrt{\frac{\lambda}{L}}. \quad (17)$$

As will be shown in the next section, the lobe positions predicted using Eqs. 15 to 17 agree well with those in the radiation antenna plots (calculated by using Eq. 10) and with the measurements. This method avoids lengthy numerical calculations in predicting traveling wave lobes. The next sections present numerical results for predicting positions of traveling wave lobes and their magnitudes, and thus derive equations which include the above results and govern the RCS contributions of traveling surface waves for a long thin rod.

NUMERICAL RESULTS FOR TRAVELING WAVE LOBES

Equations 14 to 17 can be used to calculate lobe positions and compare them with those in the antenna radiation plots (shown, for example, in Fig. 6). For an antenna having a length of 20λ , the principal lobe occurs at $\theta_1 = 11.0^\circ$, the second lobe is at $\theta_2 = 22^\circ$, and the third is at $\theta_3 = 28.5^\circ$. Substituting first the value of θ_n into Eq. 14 gives $b_1 = 1.1685$. Substituting b_1 into Eq. 13 then gives $\theta_1 = 49.4 \sqrt{\lambda/L}$ or, for the antenna of length $L = 20\lambda$, $\theta_1 = 11.05^\circ$ ($\psi = 78.95^\circ$).

This result is in a very good agreement with the plot of Fig 6. For a long antenna, such as $L = 39\lambda$, the field radiation plot is given in Fig. 7, where the principal traveling wave lobe is located at $\theta = 7.9^\circ$. Substituting this value of θ into Eq. 14 gives $b_1 = 1.1634$. This value of b_1 differs slightly from the previously calculated value. However, the value of θ_1 predicted ~~differs~~ using $b_1 = 1.1634$ in Eq. 14 for the shorter antenna ($L = 20\lambda$) agrees even better with the plot than that calculated using $b_1 = 1.1685$, found for the short antenna.

For the antenna of length $L = 5\lambda$ the first (principal) traveling wave lobe can also be accurately predicted by using Eq. 15. The location of the second or third dominant lobe can also be predicted in a similar manner. Thus from the plot of Fig. 6 (for an antenna of $L = 20\lambda$ where $\theta_1 = 21.9^\circ$) and Eqs. 14 and 16 we obtain $b_1 = 4.5898$ and $\theta_2 = 21.9^\circ$. Again comparing the predicted value θ_2 with the value from Fig. 6 reveals very good agreement. The approach developed can also be applied to derive equations and to predict the location of any traveling wave lobe. The accuracy of the predicted values of θ_n for $n > 1$ does not depend significantly on the antenna length. However for the longer antenna the predicted values of b_n and θ_n are more accurate.

The derived expressions for calculating traveling wave lobe positions in the antenna radiation pattern are used next in predicting traveling wave contributions to the RCS of a long thin rod. Comparing the radiation pattern of an antenna of length $L = 39\lambda$ (shown in Fig. 7) with the experimentally measured lobe structure in the rod RCS pattern (shown in Fig. 8) reveals remarkable similarity in the lobe structure shape, but a difference in the magnitude. The next step is to derive rod RCS equations governing the magnitude of the traveling wave lobes.

RCS EQUATIONS GOVERNING TRAVELING WAVE CONTRIBUTIONS ON A THIN ROD OF ARBITRARY LENGTH

The problem of calculating the radar cross section of a thin rod ($a \ll \lambda, L \gg \lambda$) is complicated by the presence of traveling wave returns in addition to the specular reflection. However, unlike the RCS pattern for a flat rectangular plate, on a thin rod the contributions of the two scattering mechanisms are distinct and well confined to different aspects. Specular returns manifest themselves at broadside aspect (around $\theta = 90^\circ$), while traveling waves contribute at low angles of incidence (i.e. around $\theta = 0^\circ$).

Therefore, to accurately predict the total RCS of a thin rod, the specular and traveling wave contributions must be calculated. Most earlier efforts were directed at deriving

equations governing specular reflections, and little work has been done to predict the traveling wave contributions. Since the traveling wave contributes significantly to total target RCS, an accurate and efficient method of predicting this type of scattering mechanism has been developed in this investigation. Thus in the present report we have considered only the development of equations governing the traveling wave contributions.

Peters³ first identified this problem, and he made use of antenna theory and derived RCS equations for a rod and an ogive in the region of longitudinal incidence. In the present investigation we have extended this approach to targets of an arbitrary length. Since Peters' equations include empirical value (such as current reflection coefficient γ) we developed a theoretical approach to avoid this limitation. More specifically, we consider scattering by a thin, perfectly conducting rod of arbitrary length L .

The echo area resulting from traveling waves excited on the surface of the rod is obtained by using antenna theory³:

$$\sigma = \gamma^2 A_r(\theta, \phi) \quad (18)$$

where γ is the current reflection coefficient, which depends on the antenna terminals and is found empirically, $A_r(\theta, \phi)$ is the cross section presented by the antenna to a plane wave incident from the direction θ, ϕ and is given by Eq. 19 (Silver⁷):

$$A_r(\theta, \phi) = G(\theta, \phi) \frac{\lambda^2}{4\pi} \quad (19)$$

The value $G(\theta, \phi)$ is the gain function defined as the ratio of the power radiated in a given direction per unit solid angle to the average power radiated per unit solid angle. It is independent of the actual power level and expresses the increase in power radiated by the antenna in a given direction over that from an isotropic body emitting the same total power. Here θ, ϕ are the spherical polar coordinates and λ is the wavelength. The remaining term, $\lambda^2/4\pi$, is a universal constant that represents the average absorption cross section when the antenna load is matched to its impedance (Silver⁷).

The gain function G differs for targets of different shapes. For a thin rod this function can be identified with directivity D . The directivity D is equal to the gain G for a lossless antenna and is given by Peters³:

$$D = 2B^2 / \int_0^\pi \frac{\sin^3(\theta)}{(1 - p \cos \theta)^2} \left[\sin \frac{kL}{2p} (1 - p \cos \theta) \right]^2 d\theta \quad (20)$$

where B is the maximum value of the pattern factor

$$B = \frac{\sin \theta}{1 - p \cos \theta} \sin \frac{kL}{2} (1 - p \cos \theta) \quad (21)$$

and p is the relative phase velocity of the surface current $p = v/c$; $c = 2.997 \times 10^8$ m/s, the speed of the wave in free space; $k = 2\pi/\lambda$ is the wave propagation number; λ is the

wavelength; L is the length of the target; and θ is aspect angle. (At $\theta = 90^\circ$ the incident wave is perpendicular to the target axis, and at $\theta = 0^\circ$ it is parallel to the axis).

Substituting Eq. 19 into Eq. 18 we obtain

$$\frac{\sigma}{\lambda^2} = \gamma^2 \frac{G(\theta)}{4\pi} \quad (22)$$

Approximating $G(\theta)$ to the maximum value of D given by Eq. 20 we derive the echo area resulting from traveling waves excited on the surface of a long thin target:

$$\frac{\sigma}{\lambda^2} = \gamma^2 \frac{D^2}{4\pi} \quad (23)$$

where γ is the current reflection coefficient.

The RCS equation 23 contains θ dependence which is described explicitly by Eqs. 20 and 21. It must be emphasized that to use this equation, the traveling wave lobe aspect θ_n , located at a grazing angle of incidence, must also be calculated. The location of the traveling wave lobe, i.e. the value θ_n , (for which directivity D is maximum), depends on target length and the incident wave length. Equation 15 provides the required value of θ_n .

Thus, to calculate the traveling surface wave contributions to the RCS on a thin rod of arbitrary length we use first Eq. 15 to compute the dominant lobe location θ_n for a given rod and then substitute this value into Eq. 22. A computer algorithm which includes these expressions was developed and used in our calculations to predict the traveling surface wave contributions for thin rods of various lengths. The numerical results are presented in the next section, where the computer code was used initially to calculate RCS plots for a rod for which experimentally measured data is available.

THEORETICAL AND EXPERIMENTAL RCS RESULTS FOR A LONG THIN ROD

A computer program based on the expressions presented in the previous sections was used first in the RCS calculation of the traveling surface wave on a thin rod of length $L = 39\lambda$. The measured RCS plot for a thin rod of thickness $a = 0.25\lambda$ and length $L = 39\lambda$ is available³ and was used to validate the computer code. The RCS contributions of traveling waves on the rod were calculated (Fig. 9) and compared with measurements (Fig. 8).*

Figure 8 shows the calculated and measured RCS contributions of traveling surface waves from -7.5 to $+20$ dB. The traveling surface wave lobe magnitudes decrease rapidly for aspects away from grazing angles of incidence. Traveling wave RCS contributions are dominant for aspect angles $0^\circ < \theta < 30^\circ$, while the specular reflections dominate rod radar return for aspects at and near normal incidence.

* The plot of measured data in Fig. 8 differs from the plot presented by Peters (Ref. 3, Fig. 6), who used an uneven RCS incremental step size on the y-axis. Uneven steps are cumbersome for RCS analysis and were removed to avoid confusion.

The calculated traveling wave lobe structure and RCS values agree well with measured data. In Fig. 8 these data are marked by dotted and solid lines, respectively. For the rod we also compared our calculated data with that obtained by using approximated approaches of Peters³ and Woolcock.⁹ The three calculated traveling RCS curves are shown in Fig 9. The traveling wave lobe structures calculated by these methods agree well with each other. However, our calculated traveling wave RCS peak values (shown in Fig. 9 by a solid line) are slightly higher than that of Peters and over 2 dB higher than that obtained from Woolcock equations. Since our values agree well with measurements (shown in Fig. 8) we conclude that the approach developed in the present investigation is more accurate than that of Peters and Woolcock. The latter approach can also be used for rod of arbitrary length but agrees well with measurements and our predictions for a short rod. For a rod of length 5λ the calculated traveling wave RCS values are shown in the plot of Fig. 10. Figure 10 was compared next with the traveling wave antenna radiation pattern which is shown in Fig. 7 and was also calculated for the rod of length $L = 39\lambda$.

The lobe structure and the location of individual lobes for these targets are in very good agreement. The computer code was used to predict RCS patterns for rods of various

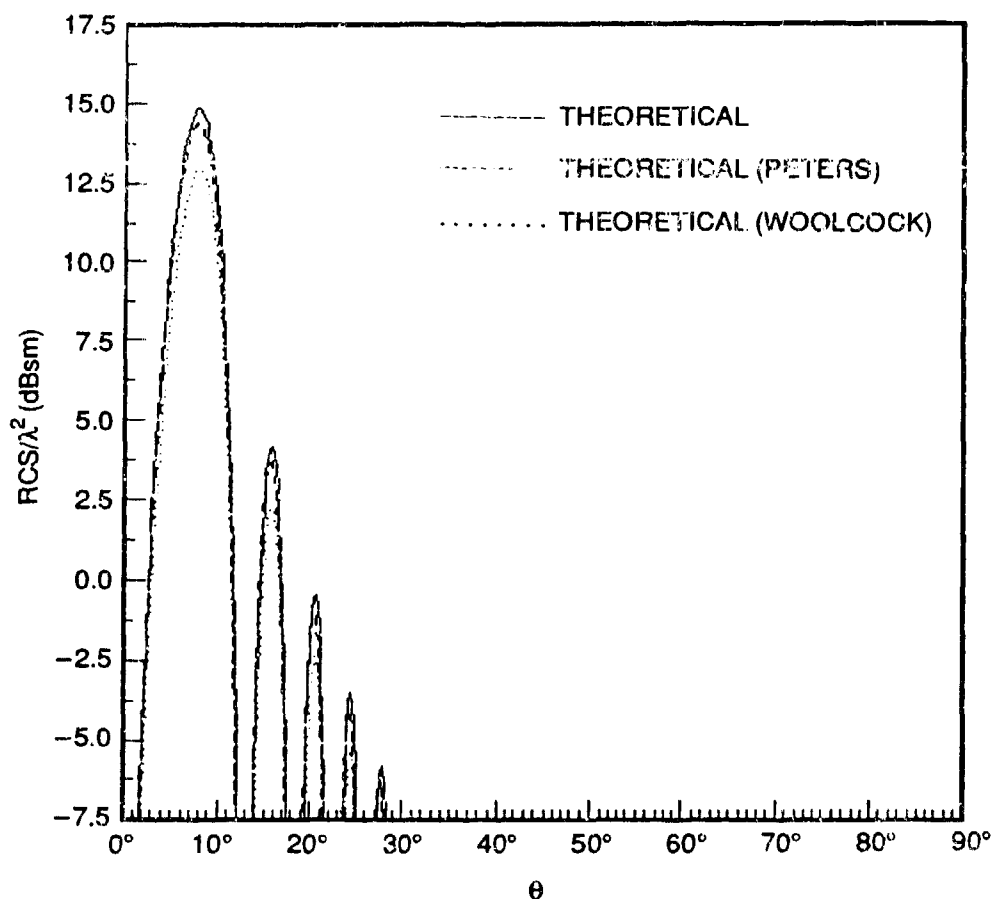


Fig. 9. Calculated traveling wave RCS contributions for a rod of length $L = 39\lambda$. Solid line was calculated using our approach, dashed line was calculated from Peters³ Eq. 7, and dotted line was obtained using Woolcock's approximated equation.⁹

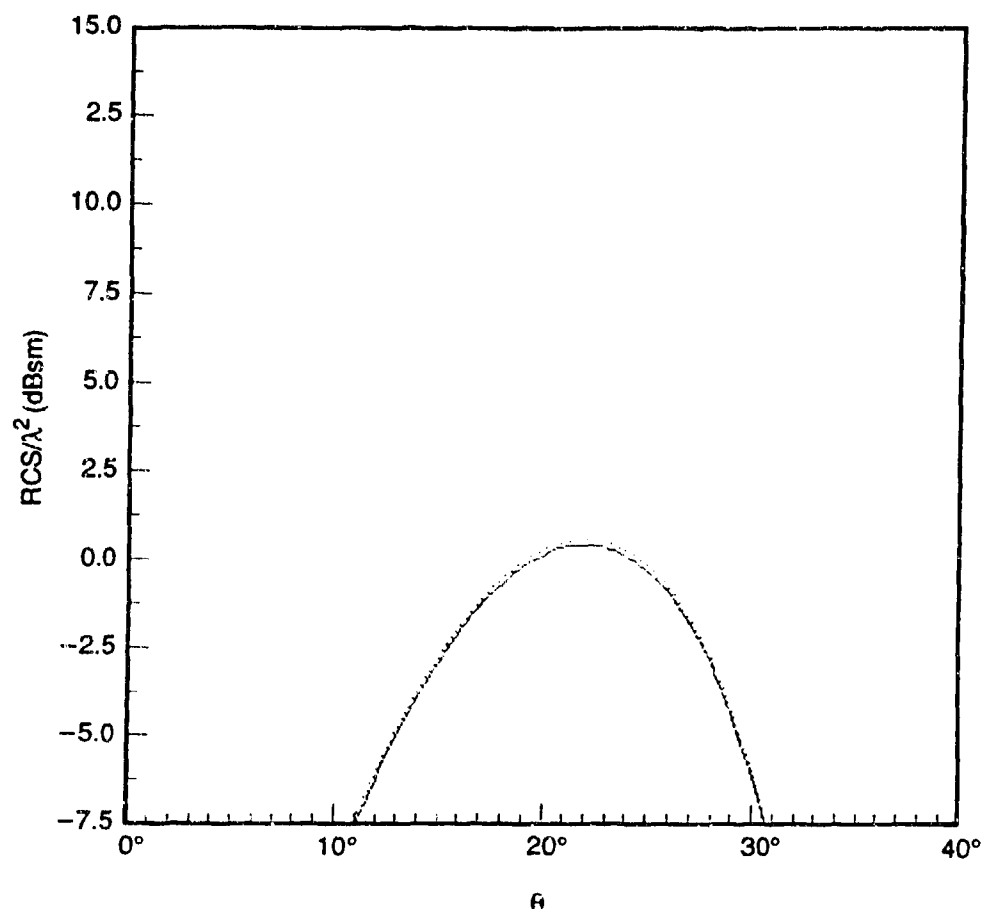


Fig. 10. Calculated traveling wave RCS contributions for a rod of length $L = 5\lambda$. Solid line was obtained by using Woolcock's approximated equation⁹, dotted line was calculated using our approach.

lengths. Figures 11, 12 and 13 show traveling wave contributions for a thin rod of length $L = 15\lambda$, 9λ , and 5λ respectively. Comparing these plots with the corresponding field pattern of Figs. 5, 4 and 3 note that the traveling wave lobe structure for the antenna agrees well with that of a rod of equal length. Thus the calculated antenna results have served well to verify the accuracy of the RCS computer code for a rod of arbitrary length.

For validation we also used the measured RCS plot for a rod shorter than that of Peters.³ Figure 14 shows calculated and measured plots for a rod of length $L = 26\lambda$. The predicted magnitude and position of the traveling wave principal lobe and the lobe structure agree well with the measurements. (The discrepancy is less than 1 dB and may come from the system used for reproduction of the measured data of Woolcock.⁹)

After validating the computer algorithm, we used it in RCS calculations of the traveling surface wave and in theory development. In the forthcoming sections we predict traveling wave contributions on a rod whose length is equal to the length of a flat rectan-

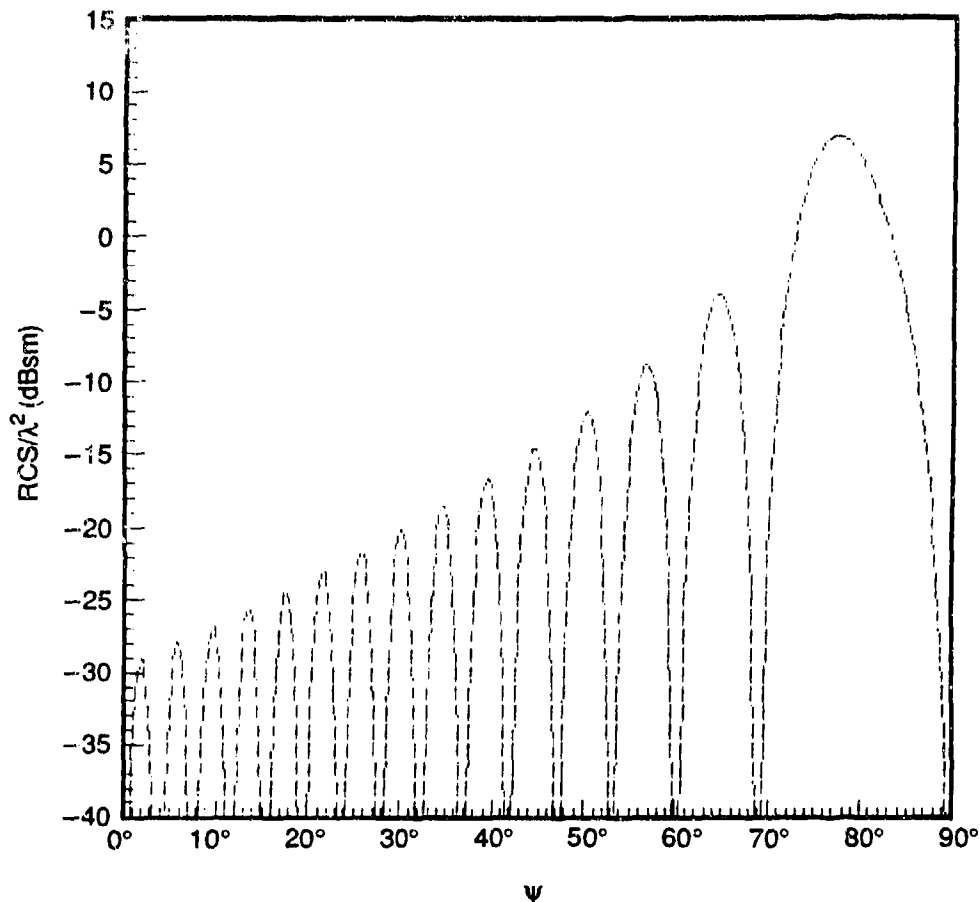


Fig. 11. Calculated traveling wave RCS contributions for a rod of length $L = 15\lambda$.

gular plate. Since for the flat plate the measured RCS data for horizontal polarization exhibit prominent traveling wave contributions, we compare it with the rod RCS plot containing the traveling wave lobe structure and RCS contributions predicted by our algorithm. We used the specific dimensions of the flat plate and the particular radar frequency that were similar to the corresponding data of Ross,⁴ who presented experimental RCS measurements. To demonstrate that the approach developed is not limited to a flat surface, we first extend it to a curved surface.

The theory of traveling surface waves can be applied to targets with a smooth curved surface. The RCS equations governing contributions of the traveling wave on an ogive is discussed next. We also compare predicted and the measured RCS plots for an ogive. After validating the computer code for calculating the RCS contributions of the traveling wave for a thick ogive, we extended our investigation to a flat plate.

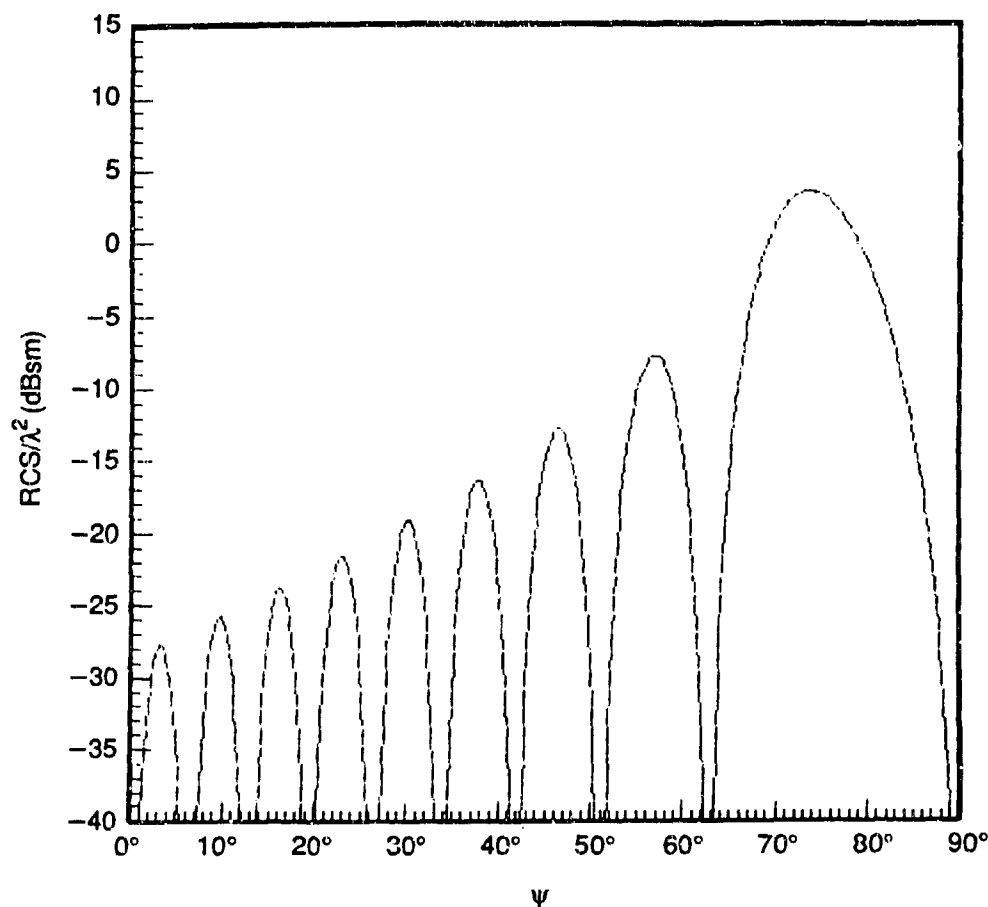


Fig. 12. Calculated traveling wave RCS contributions for a rod of length $L = 9\lambda$.

RCS EQUATION GOVERNING TRAVELING WAVE CONTRIBUTIONS ON THE OGIVE

The theory of traveling surface waves was applied to the calculation of the the RCS pattern of an ogive having arbitrary length. The ogive is a three-dimensional body defined as the minor arc of a circle of radius R rotated about its chord. The geometry of an ogive is shown in Fig. 15. Note that its geometry, though different from a rod, has many common features. Both targets have long smooth surfaces terminated by a sharp discontinuity. Hence traveling surface waves may arise during radar scattering and contribute to the target RCS signature. When the E -field component of an incident radar wave is tangential to the surface of a target and is in the plane of incidence, the surface wave is launched. It builds up as it propagates, and upon reaching the edge is reflected back. If there is no sharp discontinuity (which may be the case for some ogives) the surface wave propagates into the shadow region and emerge as a creeping wave.

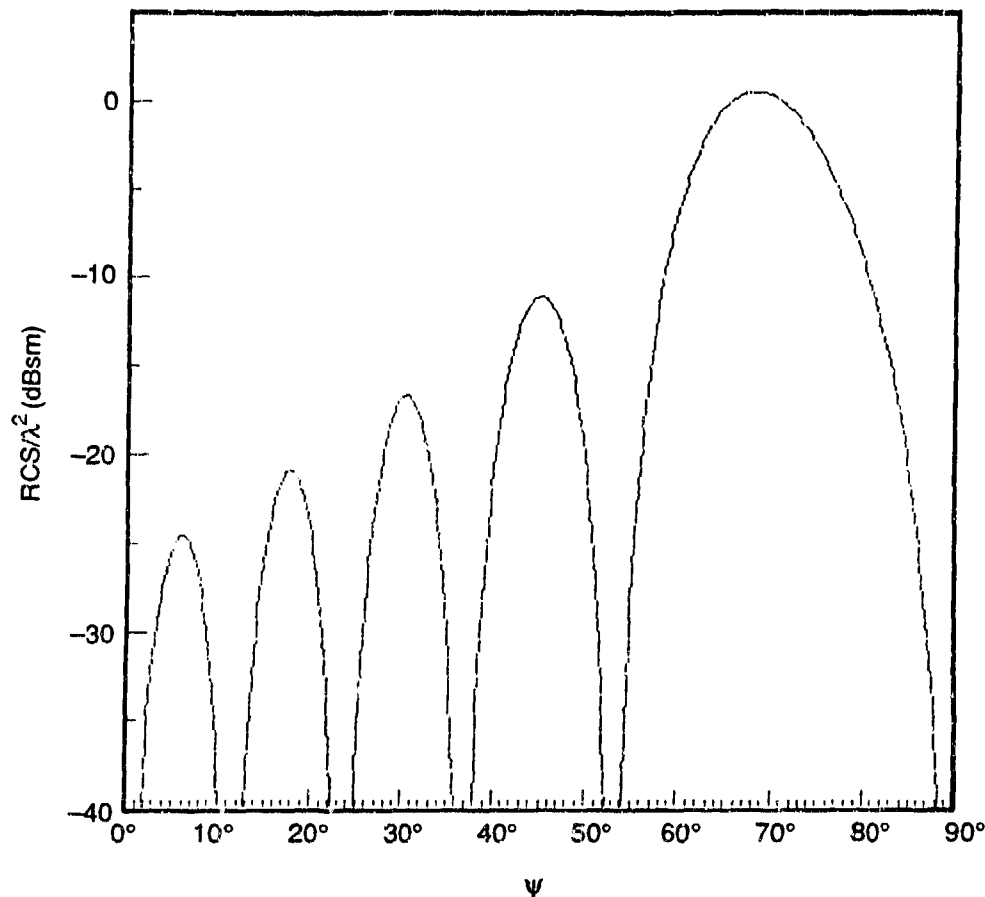


Fig. 13. Calculated traveling wave RCS contributions for a rod of length $L = 5\lambda$.

The RCS radiation pattern for this target results from specular reflection and from traveling and creeping surface waves. In contrast to end-fire antennas or thin rods which are straight, the ogive is a curved body. For such a target the axial velocity of the surface wave is somewhat slower than its velocity over the surface because of the greater distance traveled. Peters³ considered the ogive as a traveling wave antenna whose surface wave velocity is an average. The average value is assigned to the surface wave on the basis of the additional distance traveled. For an ogive the selective phase velocity of the surface current, $p = 0.99$, agrees closely with measurements.³

For an ogive of arbitrary length we first derived an expression governing the lobe structure and the amplitude of the reflected surface wave and then used that expression to calculate the traveling wave contributions to the target RCS. To derive the field patterns we adopted Peters' approach and treated an ogive as a thin linear traveling wave antenna. Then Eq. 23, which was derived for a thin rod in the previous section, is also applicable to the ogive. However, the equation for the rod (Eqs. 15 to 17) which we used to calculate

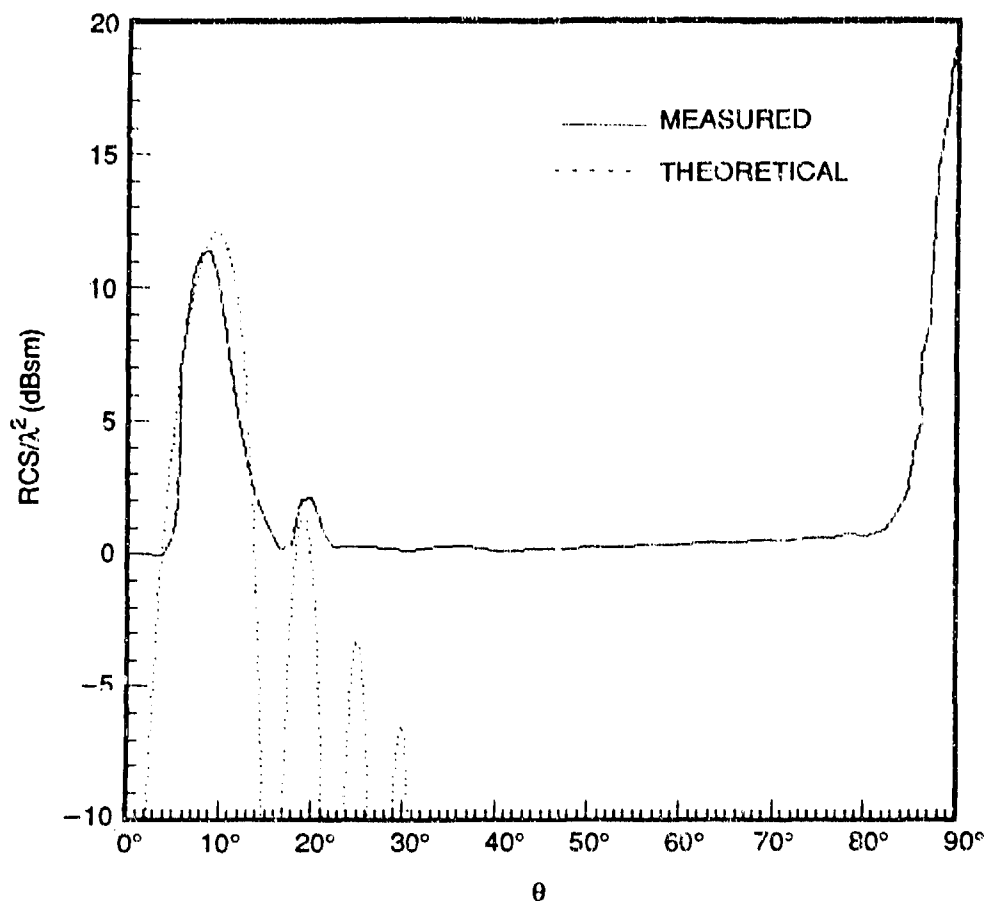


Fig. 14. Radar cross section of a rod of length 26.512λ (0.228 m), diameter = 0.00163 m, wavelength $\lambda = 0.0085$ m. Horizontal polarization. Traveling wave relative phase velocity = 1.0, and reflection coefficient = 0.32. Calculated traveling wave RCS contributions are shown by dotted line; measured curve was taken from Woolcock.⁹

the position of the principal lobes, had to be modified to account for the difference in the distance traveled by the wave on the curved surface of the ogive. For an ogive these equations become

$$\theta_1 = 49.35 \sqrt{\lambda/L_{eff}} , \quad (24)$$

$$\theta_2 = 98.09 \sqrt{\lambda/L_{eff}} , \quad (25)$$

$$\theta_3 = 127.59 \sqrt{\lambda/L_{eff}} , \quad (26)$$

where the effective length, L_{eff} , is the actual path length traveled by the surface wave on the ogive before it is scattered by the target's far end.

THEORETICAL AND EXPERIMENTAL RESULTS FOR AN OGIVE

With the ogive treated as a radar target, we are primarily interested in verifying its lobe position equations and the lobe structure in the RCS plot due to the traveling surface wave mechanism. To calculate the lobe position for the ogive shown in Fig. 15 we used Eq. 24, which accurately predicts the position of the principal lobe, the lobe structure and, together with Eq. 23, the RCS amplitude. The RCS lobe magnitude depends strongly on the current reflection coefficient γ . In our calculations for the ogive we used $\gamma = 0.7$, 0.5 and 0.32. The first value, $\gamma = 0.7$, which was obtained empirically by Peters,³ does not provide good RCS data. Because in Eq. 23 γ^2 is directly proportional to the RCS of an ogive, a smaller or larger value of γ directly leads to a decreased or increased RCS magnitude. We also used the second and third value of γ (0.5 and 0.32) to calculate the ogive RCS data and to compare it with the measurements.

The computer algorithm developed for calculating traveling surface waves on an ogive with a half-angle $\alpha = 15^\circ$ was validated with the available measured data (Peters³). Figure 16 contains measured and calculated plots for the metallic ogive of length $L = 39\lambda$, radius $R = 77\lambda$, ogive half-angle $\alpha = 15^\circ$ and frequency $f = 23.85$ GHz. In these calculations we used relative phase velocity $p = 0.99$ and the current reflection coefficient $\gamma = 0.35$. Note that Peters' published measured data for such ogive³ did not agree well with his predictions that are based on $\gamma = 0.7$. Thus, Peters' predicted plot of

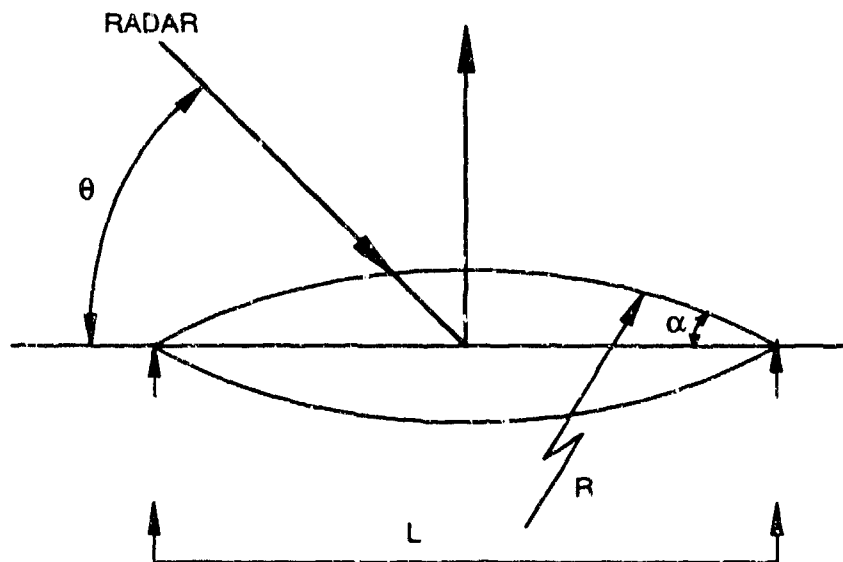


Fig. 15. Geometry of the ogive.

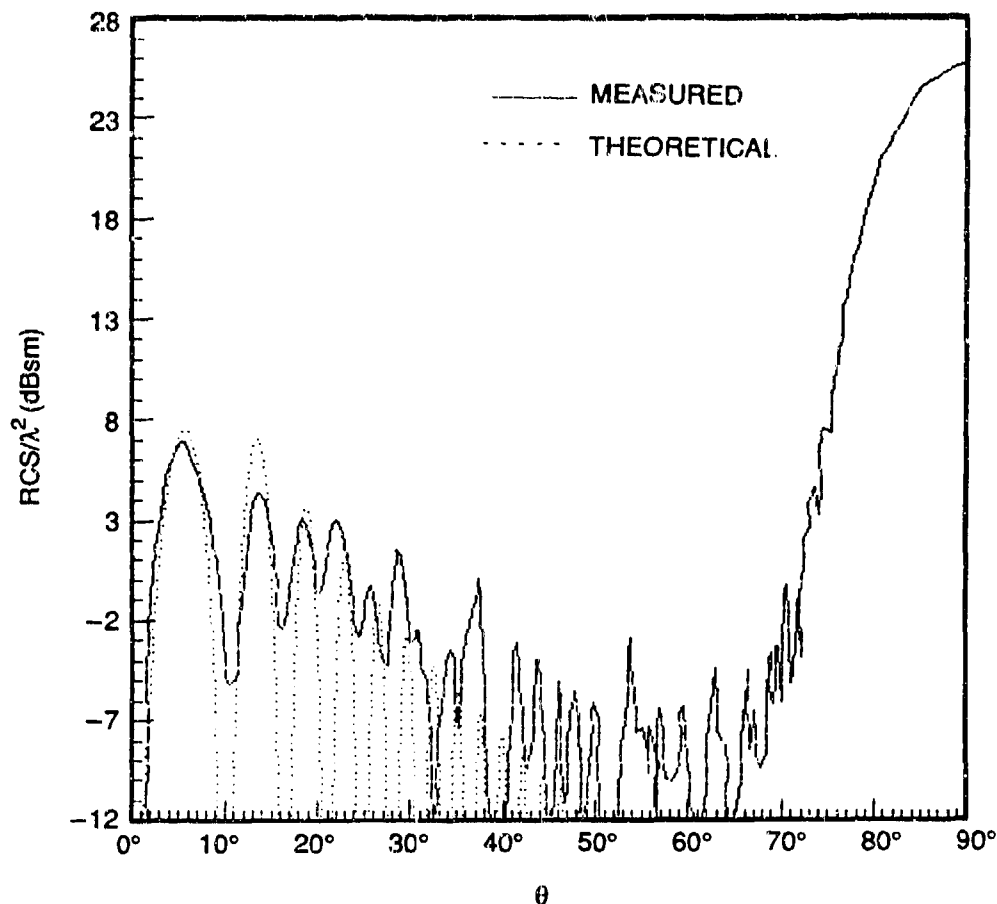


Fig. 16. Radar cross section of an ogive of length $L = 39\lambda$, (effective length 39.946λ for traveling wave), radius $R = 77\lambda$, angle $\alpha = 15^\circ$, frequency $f = 23.85$ GHz. Traveling wave phase velocity $= 0.99$, reflection coefficient $= 0.35$, horizontal polarization. Calculated traveling wave RCS contributions are shown by dotted line; measured (solid) curve was taken from Knott.⁶

RCS/λ^2 vs. θ shows over 3 dB difference from the measured values of the traveling wave dominant lobe. The y-axis of the ogive RCS radiation pattern of his Fig. 8 (Peters³), which represents values of RCS/λ^2 , was marked with nonuniform step size. This is confusing, and Knott⁶ reproduced Peters' Fig. 8 using the modified version of the plot. However, nothing was mentioned about the source of error in Peters' plot. Therefore, to validate our RCS computer program for the ogive we compared our predictions first with Eqs. 8 and 14 of Peters and then with Fig. (6-12) of Knott.⁶

The agreement is good between our calculated values of $G(\theta)$ and Peters' approximated data. The calculated values for $G(\theta)$, B , D , and kL agree very well with Peters' data if ogive length is $L = 39.95\lambda$ instead of $L = 39\lambda$. Figure 17 shows our calculated plot with a uniform step size of RCS/λ^2 values for the traveling wave on the ogive. For this plot we used the current reflection coefficient $\gamma = 0.7$ given by Peters. The lobe

structure of our plot agrees well with Peters' calculations but is higher in magnitude than his measured values. This clearly indicates that the value of $\gamma = 0.7$ is not accurate.

To predict lobe values that agree better with measurements, we used a traveling wave reflection coefficient $\gamma = 0.32$. The calculated plot for the ogive using this value of the reflection coefficient is shown in Fig. 18. Comparing this plot with Peters' measured data shows that very good agreement is achieved with $\gamma = 0.32$. Assuming that his RCS data were measured accurately, this result indicates that the traveling wave reflection coefficient is 0.32 instead of 0.7.

The other available RCS data was calculated by Maffet⁶ for an ogive of length $L = 15.19\lambda$ and the traveling wave reflection coefficient $\gamma = 0.5$. This value of γ also differs from Peters' value of $\gamma = 0.7$. Maffet used Peters' approximated equations to calculate RCS traveling wave lobes, and therefore the traveling wave reflection coefficient was still unnecessarily large. For the ogive of length $L = 15.19\lambda$ we calculated the RCS using the traveling wave reflection coefficient $\gamma = 0.25$. This plot is shown in Fig. 19.

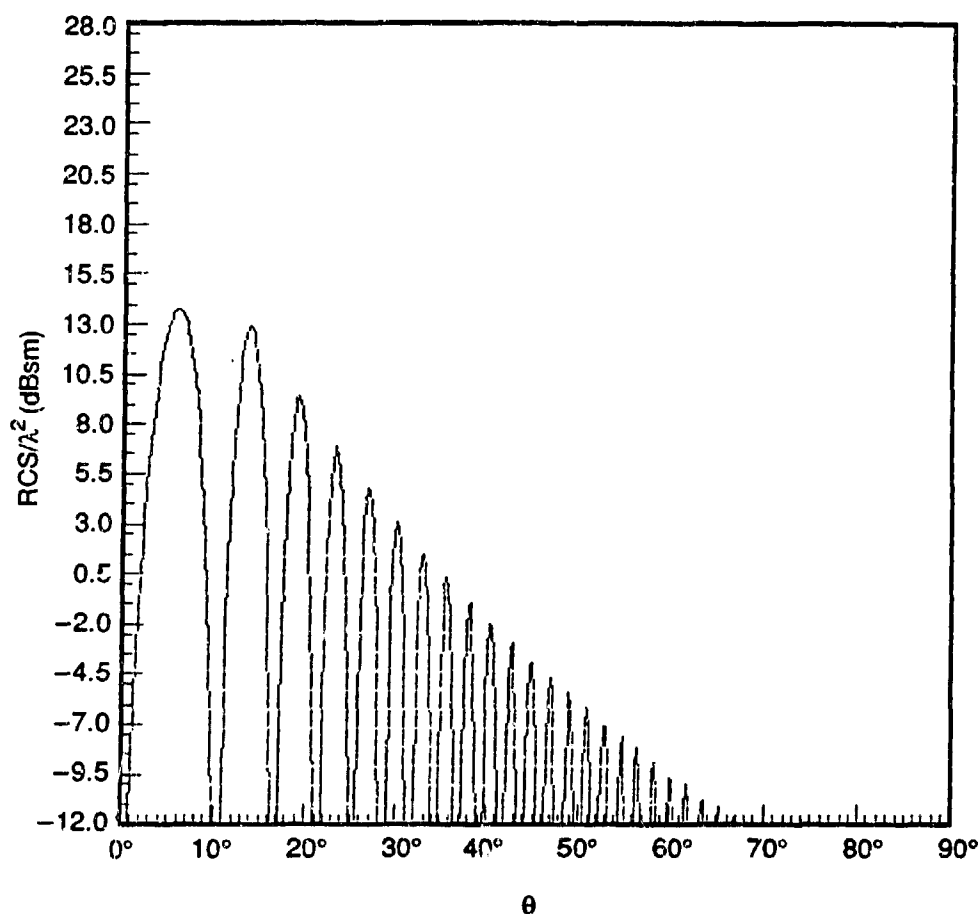


Fig. 17. Calculated traveling wave RCS of an ogive of length 39λ , radius $= 77\lambda$, ogive half-angle $= 15^\circ$, traveling wave relative phase velocity $= 0.99$, reflection coefficient $= 0.7$, frequency $= 23.85$ GHz. Horizontal polarization.

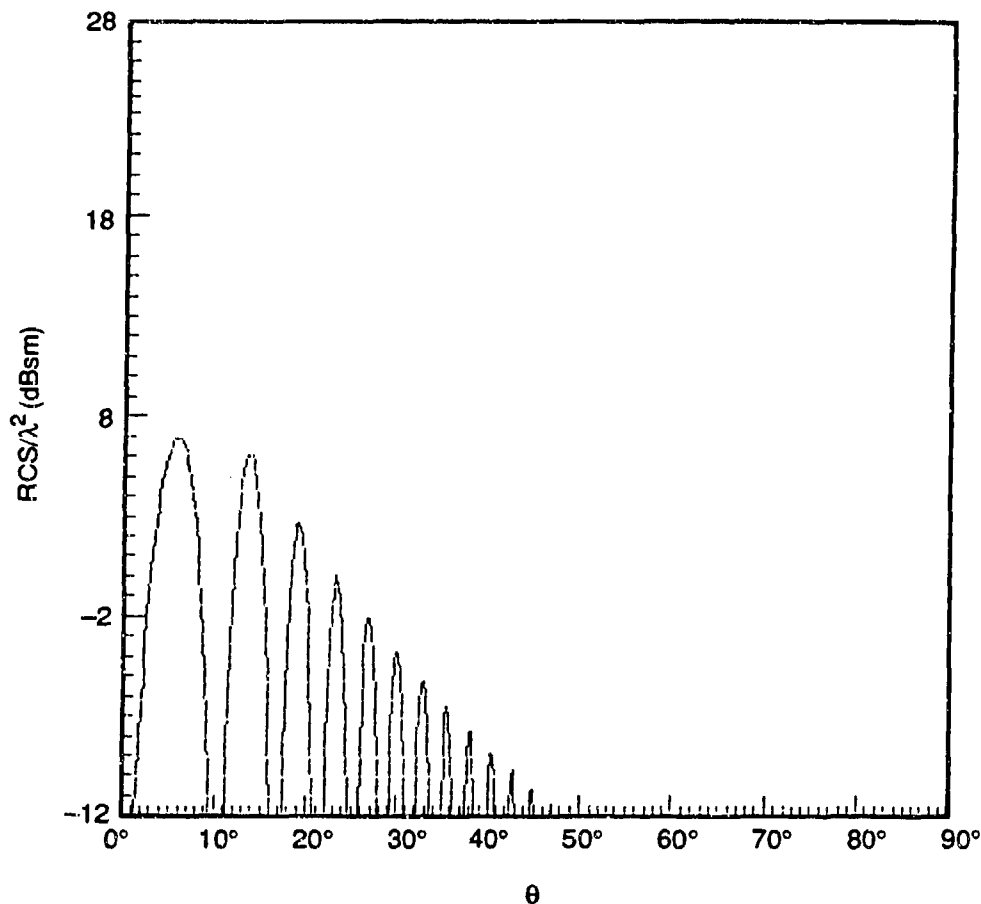


Fig. 18. Calculated traveling wave RCS of an ogive of length 39λ , radius $= 77\lambda$, ogive half-angle $= 15^\circ$, traveling wave relative phase velocity $= 0.99$, reflection coefficient $= 0.32$, frequency $= 23.85$ GHz. Horizontal polarization.

Comparison of the plot marked by dotted line with RCS values reported by Maffet⁸ (where the RCS plot was obtained using $\gamma = 0.5$) shows that the traveling wave lobe structure and the traveling wave RCS values are in very good agreement. Assuming that Maffet's plot was validated with measurements, we conclude that the correct traveling wave reflection coefficient is 0.25 rather than 0.5. Hence for ogives of lengths $L = 39\lambda$ (Peters³) and $L = 15.19\lambda$ (Maffet⁸), these reflection coefficients are 0.32 and 0.25, respectively.

We next calculated RCS for an ogive similar in shape to that shown in Fig. 15, but of shorter length (32λ), radius 62λ , and ogive half-angle 14.7° . Figure 20 shows measured and calculate RCS plots marked by solid and dotted lines, respectively. The traveling wave RCS contributions were calculated using traveling wave relative velocity 0.99 and traveling wave reflection coefficient 0.32. The measured RCS values were taken from Crispin.⁹

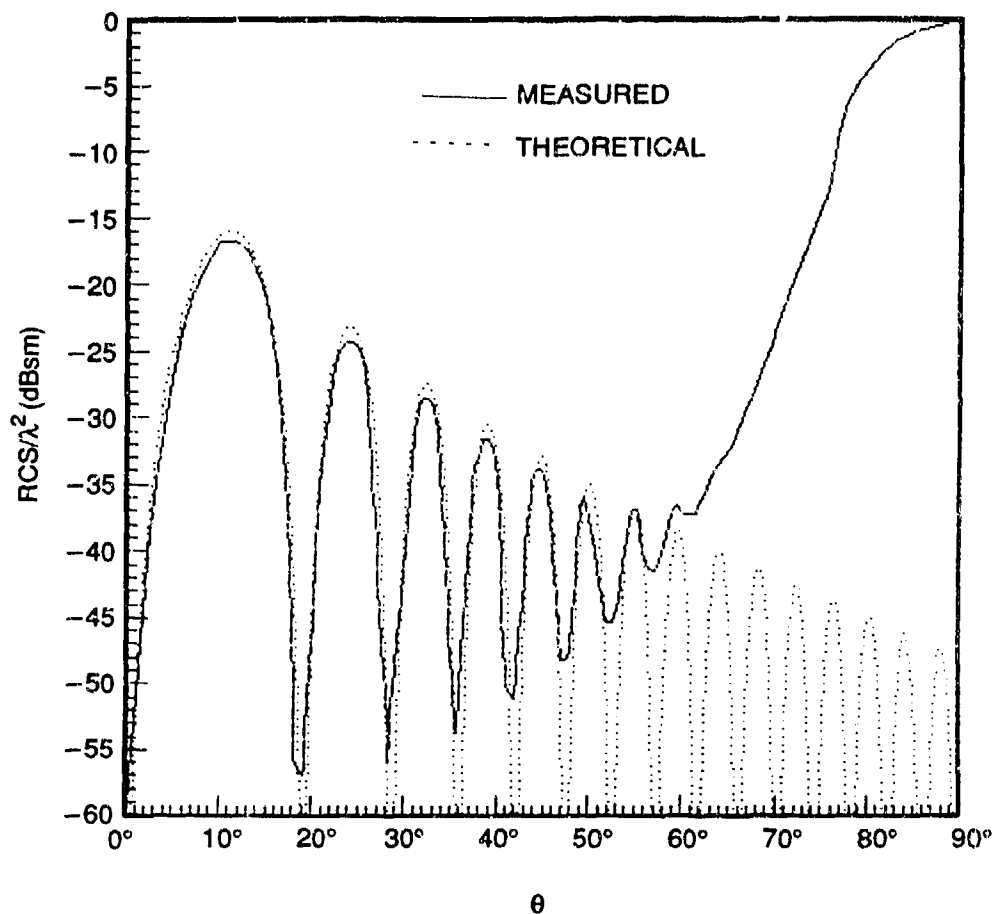


Fig. 19. Radar cross section of an ogive of length $= 15.19\lambda$ (1.519 m), radius $= 0.1$ m, ogive half-angle $= 15^\circ$, traveling wave relative phase velocity $= 0.988$, reflection coefficient $= 0.25$, frequency $= 3$ GHz. Horizontal polarization. Calculated traveling wave RCS contributions are shown by dotted line; solid curve was taken from Maffett.⁸

The calculated traveling wave lobe structure agrees well with the measurements. To compare the RCS magnitudes we shifted the measured plot to match the calculated principal lobe. The result is shown in Fig. 21. For grazing aspect angles $\theta < 50^\circ$ the traveling wave RCS contributions are dominant and predicted values agree quite well with measurements. As with the rod considered in the previous section, the specular radar returns on an ogive are dominant at and near normal incidence. Specular returns are well known and can be calculated using physical optics.^{8,10} From the comparison of the measured and the calculated plots for the three different ogives we conclude that the traveling wave reflection coefficient is larger for a longer ogive than for a shorter one. Additional measurements for ogives of different lengths and shapes (i. e. ogive R and half-angle α) are necessary to derive stable relations between the ogive length, the incident wavelength, and the traveling wave reflection coefficient. As was noted above, the traveling wave reflection coefficient affects the lobe magnitude, but does not affect the lobe structure.

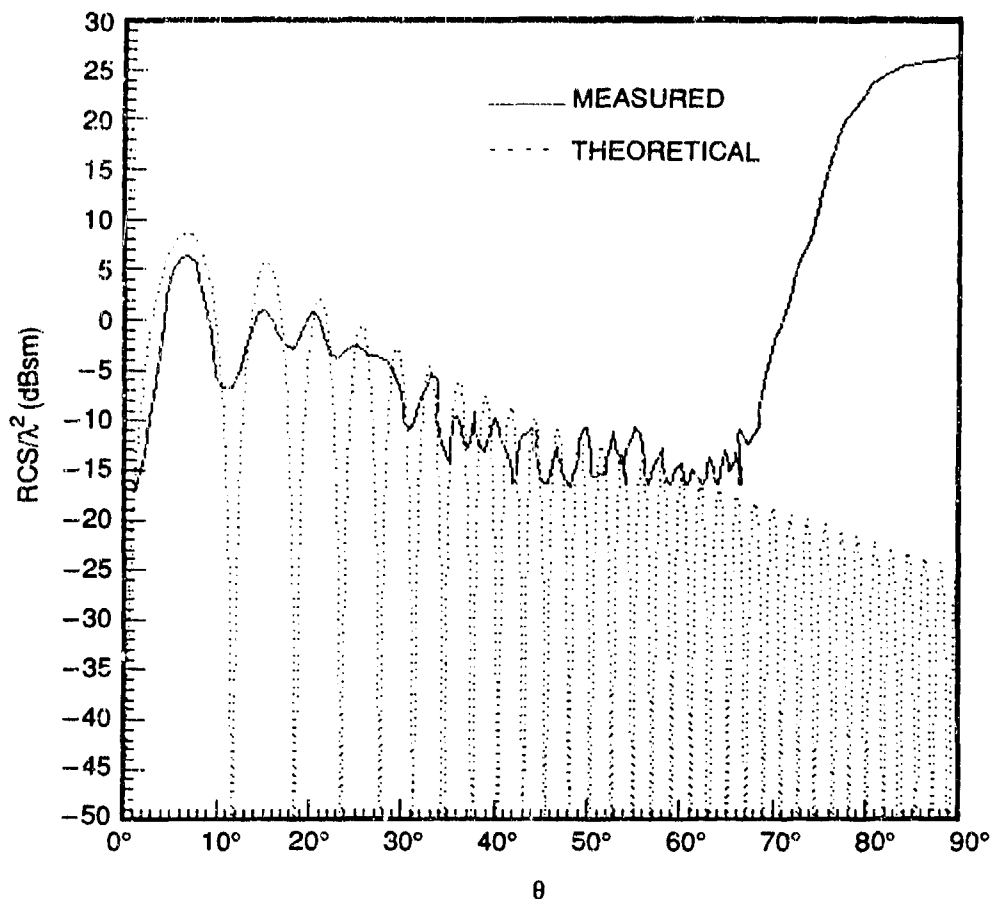


Fig. 20. Radar cross section of an ogive of length = 32λ (effective length 32.9λ), radius = 62λ , ogive half-angle = 14.6° , traveling wave relative phase velocity = 0.99, reflection coefficient = 0.32, frequency = 23.85 GHz. Horizontal polarization. Calculated traveling wave RCS contributions are shown by dotted line; measured (solid) curve was taken from Crispin.⁹

The excellent agreement between measured and predicted traveling wave lobe structures and principal lobe positions validates the approach we have developed. The RCS computer code based upon this approach predicts the traveling wave contributions quite well for an ogive of arbitrary length.

RCS RESULTING FROM TRAVELING WAVES EXCITED ON THE SURFACE OF VIRTUALLY ONE- AND TWO-DIMENSIONAL TARGETS

LINK BETWEEN THE TRAVELING WAVE ANTENNA, ROD, AND A FLAT PLATE

We have shown that a high frequency phenomenon such as the traveling surface wave is an important scattering mechanism which manifests itself through RCS contributions in the measured RCS patterns of a long thin rod and an ogive. This is also true of a flat rectangular plate, which is discussed briefly in this section and will be treated in

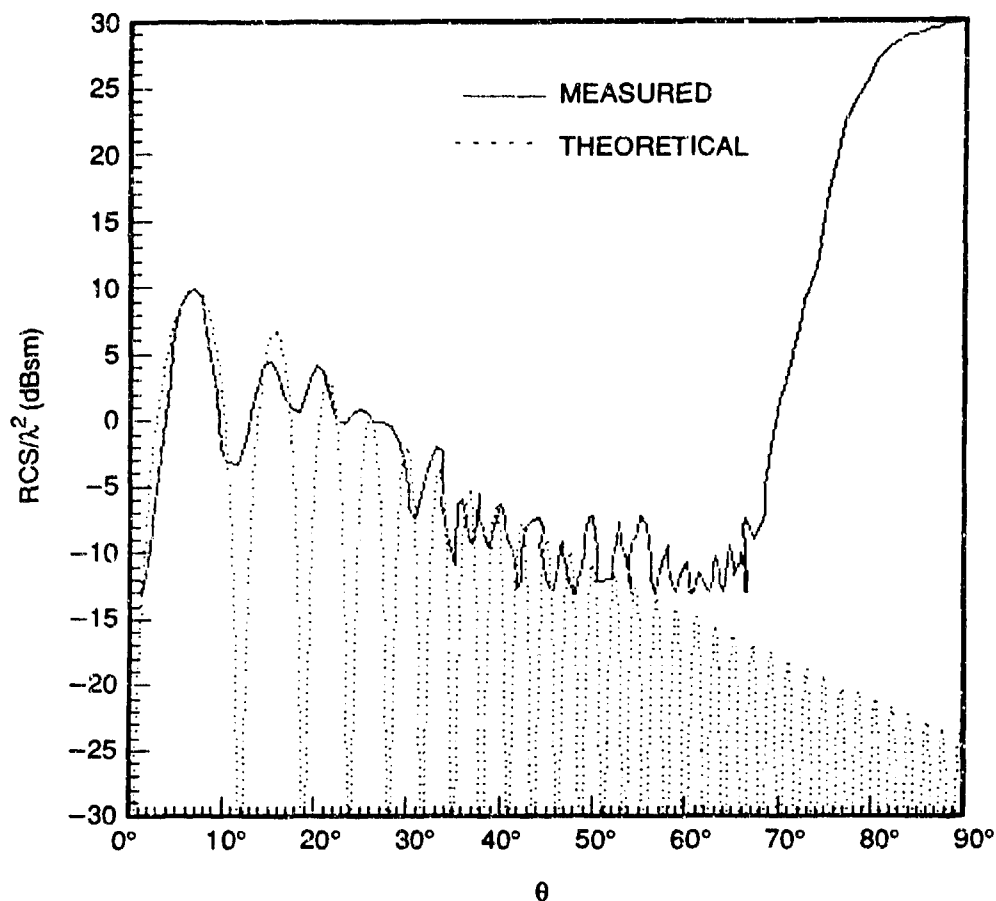


Fig. 21. Same as Fig. 20, but measured curve is shifted by 3.53 dB.

detail in a future report.* To develop the theory we began with simply shaped targets where one or two mechanisms cause radar scattering. For example, a virtually one-dimensional target such as a rod exhibits only two scattering mechanisms, specular reflection and the traveling surface wave, which dominate the total RCS pattern of the rod.

It was observed also from RCS plots that the traveling wave contributions represent a lobe structure with most of the radiation coming from the first (principal) lobe. For targets of other shapes, such as an ogive or a flat rectangular plate, more scattering mechanisms contribute to the total RCS, but the traveling wave lobe structure remains virtually unchanged. The theoretical approach developed in this report predicts accurately the location of both the principal and any other traveling wave lobes. This approach was validated and then used in RCS calculation of traveling surface waves on a thin rod of an arbitrary length. The location of the principal traveling wave lobe can be predicted by

*Stoyanov, Y.J., C.R. Schumacher, and A.J. Stoyanov, "Radar Cross Section Calculation of Traveling Surface Waves on a Flat Rectangular Plate." DTRC report in preparation.

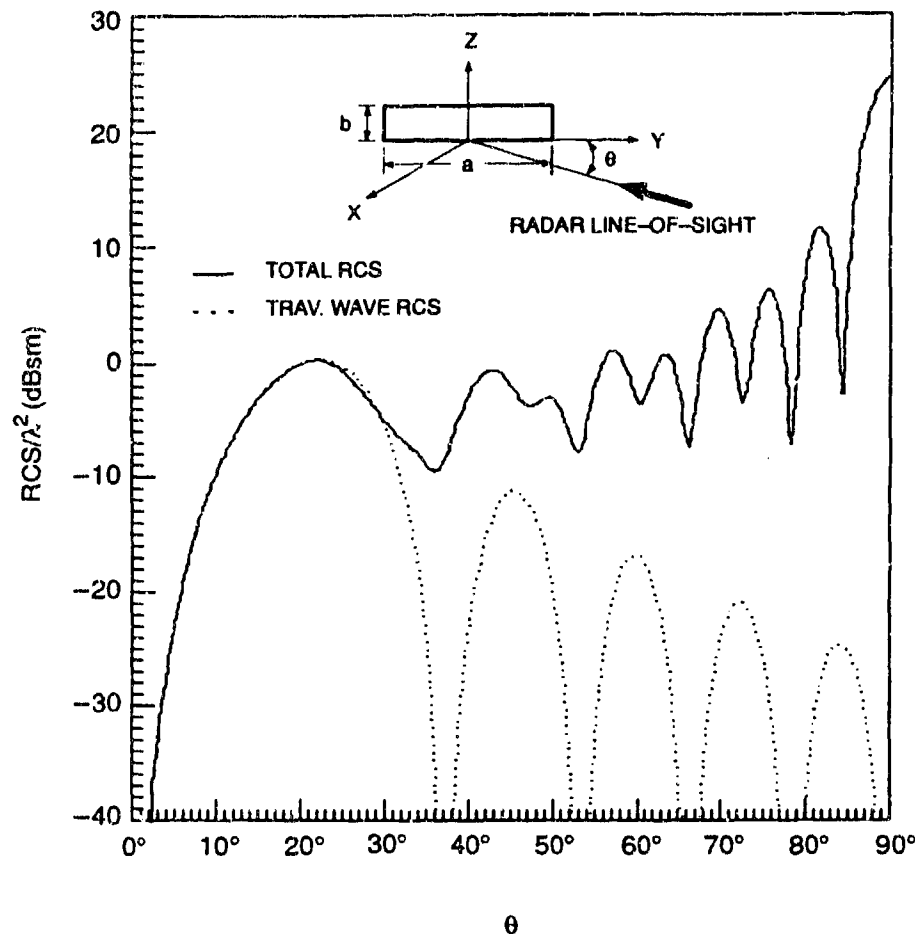


Fig. 22. Total radar cross section of a $5\lambda \times 0.9725\lambda$ flat rectangular plate (solid line) and the traveling wave RCS contributions of a rod of equal length with diameter 0.25λ (dotted line).

Eq. 15, and lobe location depends on the length of the target. With two different targets of equal length, such as a thin rod and a flat rectangular plate, it is natural to expect that the locations of the principal lobes should be the same. Our calculated RCS plots for a thin rod and a flat rectangular plate of equal length are shown in Fig. 22 and will be treated in detail in our next report. The principal traveling wave lobes for these targets agree well with each other, and clearly the traveling surface wave contributes significantly to the total RCS of the flat rectangular plate. Moreover, it can be seen from this figure that second and subsequent lobes are larger in magnitude for the plate than for the rod since additional scattering mechanisms such as diffraction effects and specular reflection contribute to the plate RCS. Specular returns for all these targets are well known and can be calculated using physical optics.^{8,10,11}

CONCLUSION

A computer algorithm has been developed which accurately calculates the contributions of traveling surface waves to the radar cross section of a thin rod and an ogive of

arbitrary length. Very good agreement with measurements was achieved. This analytical approach permits prediction and analysis of traveling surface wave lobe structure and individual lobes in these and similar targets.

In this report our prime concern was with developing the traveling surface wave theory leading toward accurate radar cross section calculation of targets of simple and complex shapes of arbitrary length. In our next reports traveling surface wave theory is developed further and is applied to calculating RCS of a number of important targets for the purpose of achieving better agreement between measured and calculated RCS data, and more effective RCS signature control and reduction.

ACKNOWLEDGMENTS

We wish to thank the Independent Research Board and Code 14 of DTRC, particularly Dr. B. E. Douglass, F. A. Halsall, W. H. Schuette, R. G. Allen, and R. H. Burns, for support and encouragement. In addition, thanks are due to M. A. Sekellick, Dr. P. Cervinka and O. M. Percy for many helpful discussions.

APPENDIX

The rms magnitude of the E-field that is described by Eq. 9 is given by:

$$\begin{aligned}
 |\mathbf{E}| &= \sqrt{EE^*} \cong \frac{\eta I_0}{4\pi r} \left(\frac{\sin \theta}{1 - \cos \theta} \right) \left[(1 - e^{-i2F})(1 - e^{i2F}) \right]^{1/2} \\
 &= \frac{\eta I_0}{4\pi r} \left(\frac{\sin \theta}{1 - \cos \theta} \right) [1 - e^{-i2F} - e^{i2F} + 1]^{1/2} \\
 &= \frac{\eta I_0}{4\pi r} \left(\frac{\sin \theta}{1 - \cos \theta} \right) [2 - 2 \cos 2F]^{1/2} \\
 &= \frac{\eta I_0}{4\pi r} \left(\frac{\sin \theta}{1 - \cos \theta} \right) \sqrt{2(1 - \cos 2F)} .
 \end{aligned}$$

Substituting $\cos 2F = \frac{e^{-i2F} + e^{i2F}}{2}$ and $1 - \cos 2F = 2 \sin F \sin F$, we obtain

$$|\mathbf{E}| = \frac{\eta I_0}{4\pi r} \left(\frac{\sin \theta}{1 - \cos \theta} \right) |2 \sin F| ,$$

or

$$|\mathbf{E}| = \frac{\eta I_0}{2\pi r} \left| \frac{\sin \theta \sin F}{1 - \cos \theta} \right| ,$$

which is presented in the text as Eq. 10.

REFERENCES

1. Knott, E. F., "A Progression of High-Frequency RCS Prediction Techniques," *Proc. IEEE*, Vol.73, No.2, pp. 252-264 (Feb 1985) .
2. For example, the AP-S International Symposium in 1986 International Symposium Digest on Antenna and Propagation, Vol. 1, IEEE Catalog No 86CH2325-9, IEEE, New York, NY 10017.
3. Peters, L., Jr., "End-fire Echo Area of Long Thin Bodies," *IRE Trans. Antennas Prop.*, pp. 133-139 (Jan 1958).
4. Ross, R. A., "Radar Cross Section of Rectangular Flat Plates as a Function of Aspect Angle," *IEEE Trans. Antennas Prop.*, Vol. AP-14, pp. 329-335 (May 1966).
5. Jackson, J. D., *Electrodynamics*, John Wiley and Sons, New York (1975).
6. Knott, E. F., J. F. Schaeffer, and M. T. Tuley, *Radar Cross Section, its Prediction, Measurement and Reduction*, Dedham, Mass., Artech House (1985).
7. Silver, S., *Microwave Antenna Theory and Design*, McGraw-Hill, New York (1949).
8. Maffet, A. L., *Topics for a Statistical Description of Radar Cross Section*, John Wiley and Sons, New York (1989).
9. Woolcock, S. C., *Target Characteristics*, E.M.I. Electronics Limited, Wells, England (Oct 1973).
10. Crispin, J. W. and K. M. Siegel, Eds., *Methods of Radar Cross Section Analysis*, Academic Press, New York (1968)
11. Ruck, G.T., ed., *Radar Cross Section Handbook*, Plenum Press, New York (1970).

INITIAL DISTRIBUTION

Copies

3 CNO
 1 Code 351
 1 Code 376
 1 Code 98
 2 ONT
 1 Code 025
 1 Code 20T (L. Schmidt)
 3 NRL
 1 Code 2600 (TID)
 1 Code 5753 (D.W. Forester)
 1 Code 5310 (G.V. Trunk)
 1 NAVAIR (C. Thomas)
 9 NAVSEA
 1 SEA 05T (R.G. Allen)
 1 SEA 5031 (W.D. Bauman)
 1 SEA 5032 (A. Summers)
 1 SEA 61R4 (H.J. Demattia)
 1 PMS 300 (J. Leonard)
 1 PMS 313 (G. Sippel)
 1 PMS 314 (A. Lee)
 1 PMS 400 (R. Staiman)
 1 PMS 400 (R. Fortune)
 2 NOSC
 1 Code 825 (J. Logan)
 1 Code 744 (M. Prickett)
 4 NSWC
 1 Code DG20 (E.J. Shuler)
 1 Code D (L.L. Hill)
 1 Code F41 (D. Marker)
 1 Code H24 (S.E. McGonegal)
 12 DTIC

CENTER DISTRIBUTION

Copies	Code	Name
1	01	R.E. Metrey
1	01ATD	D. Sheridan
1	011	H. Chaplin
1	0112	B.E. Douglas
1	0117	B. Nakonechny
1	1221	K.J. Kinports
1	14	W.H. Schuette
1	1401	R.J. Renfro
1	141	J.H. King
1	1412	M.A. Sekellick
1	1412	P.O. Cervenka
10	1412	Y.J. Stoyanov
10	1412	A.J. Stoyanov
1	1412	E.J. O'Brien
1	142	R.G. Stilwell
1	27B	C.F. Krolick
1	2751	B.R. Hood
1	284	E.C. Fischer
10	284	C.R. Schumacher
1	3411	M.L. Knox
10	3411.1	Reports Control
1	342.1	TIC (Carderock)
1	342.2	TIC (Annapolis)
1	3431	Office Services